High pressure experimental investigation of clinopyroxene dissolution in a K-basaltic melt

Barbara Bonechi[1], Cristina Perinelli[1], Mario Gaeta[1], Vincenzo Stagno[1,2], Alessandro Fabbrizio[3], Silvio Mollo[1,2], Rostislav Hrubiak[4]

1: Dipartimento di Scienze della Terra, Sapienza Università di Roma, P.le Aldo Moro 5, 00185, Rome, Italy

2: Istituto Nazionale di Geofisica e Vulcanologia, Roma - Via di Vigna Murata 605, 00143 Roma, Italy

3: Institute of Petrology and Structural Geology, Faculty of Science, Charles University, Albertov 6, 12843 Prague, Czech Republic

4: High Pressure Collaborative Access Team, X-ray Science Division, Argonne National Laboratory, 9700 S. Cass Avenue, Argonne, IL 60439, United States

Corresponding author:

Barbara Bonechi

Dipartimento di Scienze della Terra,

Sapienza Università di Roma,

P.le Aldo Moro, 5

00185 Rome, Italy

E-mail: barbara.bonechi@uniroma1.it

ORCID: 0000-0002-0242-4320

Abstract

Dissolution of clinopyroxene (cpx) in a K-basaltic melt from the Campi Flegrei Volcanic District (Italy) has been investigated through dissolution and dissolution-crystallization experiments at pressure of 0.8 GPa, superliquidus temperature of 1350 °C, and dwell times between 0.5 and 1 h. The obtained dissolution rates range from $7.9 \cdot 10^{-6}$ cm s^{-1} to $6.1 \cdot 10^{-6}$ cm s^{-1} as a function of dwell time. In the dissolution-crystallization experiment (1300 °C; 0.8 GPa; 2 h), the formation of overgrowth rims accompanied by new cpx crystals suggests that the injection of recharge magmas in basaltic reservoir may lead to inverse or oscillatory zonation. The interaction between cpx and K-basaltic melt at ~1570 °C was studied by in situ radiography using synchrotron radiation combined with the Paris-Edinburgh press. This resulted in cpx resorption to occur depending on the temperature conditions with respect to the liquidus temperature of the cpx (T_{cpxL}). The calculated cpx dissolution rates are ~$5 \cdot 10^{-3}$ cm s^{-1} at $T \leq T_{cpxL}$ and ~$3 \cdot 10^{-2}$ cm s^{-1} at $T \geq T_{cpxL}$. The role of crystal dissolution in the estimation of magma residence times has been also tested for a natural magmatic system by interpolating the dissolution rates (~10^{-5}-10^{-6} cm s^{-1}) with the textural data of cpx phenocrysts from the Agnano-Monte Spina pyroclastic deposit at Campi Flegrei caldera (Campanian region, Italy). Results from calculations indicate that the time required for partial or complete resorption of phenocrysts varies from ~0.5 to ~40 h, and that the effect of crystal dissolution may be relevant to estimate magma residence times whether significant dissolution occurs during magma mixing processes.

Keywords: clinopyroxene; dissolution rate; in situ synchrotron; high pressure; dissolution-crystallization process; Campi Flegrei

1. Introduction

Dissolution is a fundamental process in igneous petrology and it often occurs, for instance, during xenolith and/or xenocryst digestion by magma assimilation and transport processes (e.g., Edwards and Russell, 1998). The knowledge of dissolution kinetics of minerals is important to provide information and model the crystal-liquid interaction during melt transport (Kelemen, 1990; Navon and Stolper, 1987; Reiners, 1998). Among the studies available in literature on mineral dissolution in silicate melts, those focusing on clinopyroxene (cpx) are few (Chen and Zhang, 2009; Kuo and Kirkpatrick, 1985a; Kutolin and Agafonov, 1978; Scarfe et al., 1980; Van Orman and Grove, 2000; Zhang et al., 1989) (Fig. 1), and only those by Brearley and Scarfe (1986) and Scarfe et al. (1980) report data on cpx dissolution in alkali basaltic compositions. Crystal dissolution in silicate melts can be controlled by interface reaction and mass transfer, with this latter mechanism being both convective (e.g., Kerr, 1995; Liang, 2003; Zhang and Xu, 2003) and diffusive (e.g., Liang, 1999; Zhang et al., 1989). Crystal dissolution in nature often occurs under convective conditions driven by density differences between crystals and melt, or density differences between interface and far-field melts (e.g., Chen and Zhang, 2009, 2008; Kerr, 1995; Shaw, 2000). Convective dissolution has been investigated in some early experimental works (e.g., Brearley and Scarfe, 1986; Donaldson, 1985; Kuo and Kirkpatrick, 1985b) showing that the dissolution rate does not depend on the crystallographic orientation but scales with dwell time. However, as pointed out by Zhang et al. (1989), convective dissolution cannot be used to quantify chemical diffusivities, and the application of dissolution rate is restricted to natural systems with similar convection regimes. To overcome this limitation, more recently the effects of non-convective dissolution have been investigated (e.g., Finnila et al., 1994; Liang, 2000, 1999; Morgan et al., 2006; Shaw, 2006; Watson, 1982; Zhang et al., 1989), pinpointing that diffusive mass transfer and dissolution rates are inversely proportional to the square root of time. Generally, the crystal dissolution rate is studied by assuming an effectively

semi-infinite or infinite reservoir. However, crystal dissolution measured in a finite geometry (e.g., partially molten system) can provide useful information about specific magmatic processes such as melt-rock reactions occurring at the edges of magmatic reservoirs between melt and cumulitic rocks (e.g., Liang, 2000; Morgan and Liang, 2003; Tursack and Liang, 2012). Melting and dissolution of minerals are important processes in petrogenesis of igneous rocks (e.g., magma genesis by partial melting, assimilation of xenoliths, resorption of minerals during magma mixing; Tsuchiyama, 1986). As general statement, melting of a crystal occurs when the temperature is above the liquidus of the crystal phase regardless of whether or not a melt or fluid is present while "partial melting occurs when the temperature is between the solidus and liquidus" (Zhang, 2008) of the crystal phase. Dissolution of a crystal requires instead the presence of a melt or fluid that is undersaturated with the crystal and occurs when the temperature is below the solidus of the crystal phase. In this study, we report the results from three different types of experiments: 1) dissolution experiment in a semi-infinite reservoir, 2) dissolution-crystallization experiment in a finite reservoir, and 3) in situ dissolution experiment at $T \geq T$ liquidus of clinopyroxene. Through experiments 1) and 2), we investigated clinopyroxene dissolution and dissolution-crystallization in an alkali basalt at the pressure of 0.8 GPa, superliquidus temperatures of 1300 and 1350 °C, and dwell times between 0.5 and 2 h. Through experiment 3), we observed in situ the cpx dissolution at ~1570 °C and 2 GPa. Data obtained from dissolution experiments were used to quantify crystal dissolution rates in a K-basaltic melt. Cpx dissolution rates from this study were finally employed to determine phenocryst residence times and magma chamber dynamics at Campi Flegrei caldera (Campanian region, Italy).

2. Experimental and analytical methods

2.1. Starting materials and experimental design

97 The starting material for the reacting melts used in this study (Table 1) is a natural rock powder
98 obtained from a K-basaltic (APR16; D'Antonio et al., 1999) scoria clast included in the deposits
99 of Solchiaro hydromagmatic eruption (between 19±6 ka and 14±3 ka; Morabito et al., 2014)
100 located in Procida Island (Campi Flegrei, Italy). It is characterized by 12 vol.% of forsteritic
101 olivine (ol) and diopsidic cpx phenocrysts dispersed in a groundmass of ol, cpx, plagioclase
102 (plg), oxide (ox), alkali feldspar (afs) and glass (D'Antonio et al., 1999; De Astis et al., 2004).
103 The powder, used as starting material in the APR16-D1Ab run, was obtained by grinding the
104 APR16 rock sample in an agate mortar under acetone. A synthetic glass, used as starting material
105 in the other runs, was prepared by melting the APR16 natural powder at 1400 °C and oxygen
106 fugacity corresponding to the NNO (nickel-nickel oxide) buffer for 15 min in a gas-mixing (CO-
107 CO_2) furnace installed at the Bayerisches Geoinstitut (Bayreuth, Germany) (Bonechi, 2020;
108 Bonechi et al., 2020a, 2020b). The quenched glass, named APR16GL was then ground in an
109 agate mortar under acetone. The two starting materials were dried at 110 °C for at least 2 h to
110 remove the moisture before being loaded in the $Au_{75}Pd_{25}$ capsules. The used clinopyroxenes are
111 natural homogeneous diopsidic crystals (hereafter cpx Ves; Wo_{48}-En_{46}-Fs_6 and Mg# = 0.90, with
112 Mg# = MgO/(MgO+FeO_{tot}) on molar basis by assuming all iron as FeO_{tot}) from the 1944
113 Vesuvius eruption (Morgan et al., 2004) (Table 1). These crystals were chosen because *i*) they
114 are not in equilibrium with the APR16 melt (Perinelli et al., 2019), thus simulating dissolution
115 mechanisms due to the effect of temperature change and mixing between magmas with different
116 degrees of differentiation, and *ii*) can be easily hand-picked as idiomorphic single crystals and
117 further worked into the desired shape. Thus, cpx crystals were cut and ground in small
118 parallelepiped shapes (~1×1×0.5 mm) and polished. For all the experimental runs performed
119 with the piston cylinder and the Paris-Edinburgh press, we used the same procedure to place the
120 cpx Ves, with a set up that does not allow to control convection but guarantees isothermal-

isobaric conditions. In particular, we packed the bottom of the capsule with a thin layer of powdered basalt, on which the cpx Ves grain was positioned covered by a further thicker layer of powdered basalt (Fig. S1 in Online Resource 1). For each experiment, the cpx Ves was oriented placing it with the c-axis parallel to the bottom of the capsule in the APR16-D1Aa and APR16-D1Ab runs, and perpendicular to it in APR16-D1A run, in order to point out possible anisotropies of the cpx–melt interface reaction. The orientation of the crystals was marked by welding a Pt-wire on the outer wall of capsule. This procedure allowed to recognize possible shifts from the pristine orientation of crystal during the experiment (see § 2.4. *Analytical methods*). In APR16-D1Ab run, we used a cpx Ves with larger dimensions (1.4x2.2x2.3 mm) than the other ones, reducing the powdered starting material/cpx Ves ratio (Table 2). This latter experimental procedure implies a finite geometry system, and the chemical system shifts towards the cpx composition. The increase of the cpx components activity (i.e., chemical components) in the melt phase, due to variable cpx dissolution, holds to an increase of the liquidus temperature of the system (according to the depression of the melting point). Consequently, the system is forced to stay close to the liquidus temperature and small variations of the melt composition, due to the diffusion of dissolved components, can produce local crystallization of cpx whose composition is stable at high temperature (i.e., Mg-rich cpx).

2.2. Experimental procedure

Experiments were performed by using the ½ inch end loaded piston cylinder apparatus (PC) at the HP-HT Laboratory of the Department of Earth Sciences of Sapienza - University of Rome (Italy), and the VX-3 Paris–Edinburgh press (PE) at the 16-BM-B beamline (HPCAT) at the Advanced Photon Source (Argonne National Laboratory, Illinois). Four experiments were carried out with the PC at the isobaric pressure of 0.8 GPa, dwell times between 0.5 and 2 h, and

temperatures of 1300 and 1350 °C, corresponding to ΔT of 20 and 60 °C, where ΔT ($T_{experiment}$ - $T_{liquidus}$) is the difference between the nominal temperature of the runs and the APR16 liquidus temperature (Table 2). One of the experiments failed and excluded. Temperature conditions were chosen to be *i*) higher than the liquidus temperature of the basalt (i.e., 1280 °C for the APR16 sample at 0.8 GPa, as reported in Perinelli et al. (2019)) to avoid crystallization in the bulk melt that disturbs the diffusion and dissolution processes, and *ii*) lower than the melting temperature of the diopsidic cpx at 0.8 GPa (i.e., 1495 °C for pure diopside, in agreement with Boyd and England (1960), Williams and Kennedy (1969) and Yoder (1952), as well as 1425 °C for the cpx Ves calculated using the software MELTS (Ghiorso and Sack (1995)) (Fig. 1; Table 2). The PC assembly (Fig. S1a in Online Resource 1) consists of an outer CaF_2 cell, graphite furnace and MgO crushable spacer. Temperature was measured using a D-type W_3Re_{97}-$W_{25}Re_{75}$ thermocouple and manually controlled within an uncertainty of ±5 °C. Capsules of less 7-mm long were used in order to maintain the samples in the furnace hot spot. The experimental assembly was first pressurized to the target pressure by piston-out procedure (Johannes et al., 1971; Presnall et al., 1978). An overpressure of ~10% was applied with increasing temperature and corrected for pressure drops due to stress relaxation within the assembly during heating. The assembly was heated up to the target temperature with a rate of 150 °C min^{-1}. The sample was maintained at the pressure and temperature for a given duration (nominal duration), and then quenched down by turning off the power. The in situ experiment was performed using the PE press at 2 GPa, ~1570 °C and dwell time of 4 s (Table 2). The PE cell assembly (Fig. S1b in Online Resource 1) mainly consists of boron-epoxy (BE) gaskets, MgO ring, ZrO_2 cap, graphite heater, and BN capsule. Graphite inner capsule was used for silicate melt experiments inside BN sleeve (Kono et al., 2014a). A ring-shaped BE (boron: epoxy = 4:1 in weight ratio) is used as gasket with a supporting outer polycarbonate plastic (Lexan) ring. The BE gasket and ZrO_2 caps

in the assembly provide good thermal insulation for high temperature experiments. The MgO ring is placed between BE gasket and graphite heater to increase the stability of the cell assembly and maintain anvil gap. The MgO ring is also used as the pressure standard, according to the thermal equation of state by Kono et al. (2010). The pressure uncertainty is ±0.2 GPa. The loaded cell was first brought to the target pressure by a hydraulic system connected to the Paris-Edinburgh press. After pressurization, the sample was heated rapidly at a rate of ~100 °C s^{-1}. The temperature was estimated using the electrical power vs. temperature calibration curve reported in Kono et al. (2014a) with uncertainty of ~60 °C (Kono et al. 2014b). The experiment was quenched by shutting down the electrical power to the heater.

2.3. Ultrafast X-ray imaging with the Paris Edinburgh press

For the PE experiment, a white X-ray radiography was used to photomicrograph the interior of the capsule at high pressure. In particular, the dissolution rate of the cpx Ves in the APR16-D1 run was measured by a collimated (1.5x1.5 mm) white X-ray beam and radiographic photomicrographs captured by a high-speed camera (Photron FASTCAM SA3) with 250 frame per second (fps) recording time with pixel resolution of 2.5 μm/pixel (Kono et al. 2014a). The radiographic photomicrographs were collected during heating of the run until the dissolution of the cpx Ves was observed. Figure S2 in Online Resource 1 is a radiographic photomicrograph showing the initial position of the cpx Ves in the middle part of the starting sample, and inside the graphite cap at the top of the capsule. Movie 1 in Online Resource 2 shows, in real time, the dissolution of the cpx Ves in the APR16GL melt at 2 GPa and ~1570 °C over a time duration of ~4 s.

2.4. Analytical methods

193 The recovered samples were mounted in epoxy resin, ground flat, and polished. Textural features
194 of the experimental runs were analyzed by scanning electron microscopy (SEM) using a FEI-
195 quanta 400 equipped for microanalysis with an EDAX Genesis system at the Department of
196 Earth Sciences of Sapienza - University of Rome and a TESCAN Vega equipped with EDS
197 (energy dispersive X-ray spectrometry) system at the Institute of Petrology and Structural
198 Geology of the Charles University in Prague (Czech Republic). We also analyzed the phase
199 compositions by electron probe micro-analysis (EPMA) using a Cameca SX50 equipped with
200 five-wavelength dispersive spectrometer (WDS) and installed at CNR - Istituto di Geologia
201 Ambientale e Geoingegneria in Rome (Italy). A 15 kV accelerating voltage, 15 nA beam current,
202 and the following standards were used: metals for Mn and Cr, jadeite for Na, wollastonite for Si
203 and Ca, orthoclase for K, corundum for Al, magnetite for Fe, rhodonite for Mn, rutile for Ti,
204 periclase for Mg, apatite for P. Counting times were 20 s for elements and 10 s for backgrounds.
205 Light elements were counted first to prevent loss by alkali migration. Raw data were corrected
206 using the PAP method. We analyzed minerals using a beam diameter of 1 μm, and glasses (single
207 spot analyses) with a defocused beam from 10 to 15 μm of diameter. For each experiment,
208 multiple compositional profiles were measured by using a Jeol JXA-8530F equipped with five
209 wave dispersive spectrometers (WDS) at the Institute of Petrology and Structural Geology. The
210 operating conditions were 15 kV and 15 nA beam current. Standards were quartz for Si,
211 corundum for Al, periclase for Mg, magnetite for Fe, rhodonite for Mn, calcite for Ca, rutile for
212 Ti, chromium oxide for Cr, albite for Na, apatite for P. Profiles across cracks are re-connected
213 smoothly. First, we made preliminary profiles by measuring points with a distance of 5 μm and
214 a beam diameter of 1 μm. Subsequently, to better define the area at the cpx-melt interface, we
215 made other profiles parallel and close to the first ones using a distance and a beam diameter of 1
216 μm. Crystallographic orientations of the polished residual cpx Ves were obtained by electron

backscatter diffraction (EBSD) at the Institute of Petrology and Structural Geology. EBSD patterns were collected with an accelerating voltage of 20 kV, beam current 6 nA, working distance of 33 mm, and tilt angle of 70°. On each cpx Ves, 10 points were analyzed, all of which produced a good indexed solution for diopside using AZtec software, with a mean angular deviation <0.5°. Averaged results are shown in Figures 2, 3 and S3 in Online Resource 1 as equal-area upper-hemisphere projections of the crystallographic axes.

3. Results

3.1. Textural and chemical features of the experimental runs

Textural and chemical aspects of the experimental runs are described in the following two sections: "Dissolution experiments" and "Dissolution-crystallization experiment". In the first section we focused on the APR16-D1A, APR16-D1Aa, and APR16-D1 runs. In the second section, instead, we focused on the APR16-D1Ab run, that is characterized by a more complex dissolution-crystallization process. The compositions of minerals and those of glasses far from the residual cpx Ves (at distance $x \geq 500$ μm) for all the runs are reported in Table S1 in Online Resource 3. Compositional profiles conducted at the interface ($x = 0$ μm) between cpx Ves and glass for the APR16-D1Aa, APR16-D1A, and APR16-D1Ab runs are reported in the Electronic Appendix in Online Resource 4. The compositional profiles show that SiO_2, MgO, and CaO of the glass increase, whereas TiO_2, Al_2O_3, FeO, Na_2O, and K_2O decrease towards the cpx-melt interface. In the far-field melt, instead, the compositional profiles are flat, and no compositional gradients can be observed. According to Zhang et al. (1989) and Chen and Zhang (2008, 2009), we observe a bent profile very close to the cpx-melt interface that can be attributed to the overgrowth of tiny cpx crystals on the pre-existing crystalline surface at the time of quench (Fig. A4 of Electronic Appendix in Online Resource 4). The bent part of the profile is indeed

consistent with cryptic overgrowth of cpx, as the interface melt becomes supersaturated with newly-formed cpx crystals during quench (Yu et al. 2016).

3.1.1. Dissolution experiments

Cpx Ves of APR16-D1Aa run (1350 °C; 0.8 GPa; 0.5 h) shows subrounded edges without reaction texture. This suggests that dissolution occurred during the experiment according to Tsuchiyama (1986). One side of the crystal displays some indentations (Fig. S4a in Online Resource 1). Similarly, in APR16-D1A run (1350 °C; 0.8 GPa; 1 h) the cpx Ves shows a subrounded shape with indentations on one side, in front of which the formation of ol and ox occurred (Fig. S4b in Online Resource 1), probably linked to the presence of small inclusions in the cpx Ves. As regards the APR16-D1 (~1570 °C; 2 GPa) experiment, the radiographic Movie in Online Resource 2 shows the complete dissolution of cpx Ves. Crystal dissolution starts from the edges and the corners of the grain, leading to a round shape before its complete disappearance. The composition of the residual cpx Ves in APR16-D1Aa run (1350 °C; 0.5 h) does not differ significantly from the original one (Fig. 4). Conversely, the residual cpx Ves in the APR16-D1A run (1350 °C; 1 h) shows higher Mg# (0.91) and lower TiO_2 (0.29 wt.%), Al_2O_3 (1.43 wt.%), and Cr_2O_3 (0.22 wt.%) than the original cpx Ves (Table 1 and Table S1 in Online Resource 3). Concerning the experimental glasses, those analyzed far from the residual cpx Ves of APR16-D1A and APR16-D1Aa runs have major oxide concentrations similar to those of the starting material (APR16GL; Fig. 5), while the composition of APR16-D1 glass exhibits higher Mg# (0.73) and CaO abundances (12.9 wt.%) reflecting the complete dissolution of the cpx Ves in the melt (Movie 1 in Online Resource 2). The Fe–Mg exchange between cpx Ves (within 50 µm from the edge; Electronic Appendix in Online Resource 4) and melt far from the cpx-melt interface ($K_D(\text{Fe-Mg})^{cpx\text{-}liq} = Fe_{cpx} \times Mg_{liq}/Mg_{cpx} \times Fe_{liq}$, calculated assuming all Fe as Fe^{2+} in both

phases) for APR16-D1Aa and APR16-D1A runs is 0.26±0.01 and 0.24±0.01, respectively. These values indicate that reacted cpx Ves are in equilibrium with the coexisting melt according to the equilibrium criteria (K_D(Fe-Mg)$^{cpx\text{-}liq}$ = 0.28±0.08) proposed by Putirka (2008). Finally, in the APR16-D1A experiment, ol and ox crystallize during cpx dissolution. Ol is characterized by a homogeneous composition (Fo_{93}). Conversely, ox is compositionally zoned, with core enriched in Fe_2O_3 and MgO relative to the magnesioferritic rim. The Fe–Mg distribution coefficient between ol and melt (K_D(Fe-Mg)$^{ol\text{-}liq}$ = Fe_{ol}×Mg_{liq}/Mg_{ol}×Fe_{liq}, calculated assuming all Fe as Fe^{2+} in both phases) is 0.17±0.03, thereby in disequilibrium with the melt according to the criteria (K_D(Fe-Mg)$^{ol\text{-}liq}$ = 0.30±0.03) proposed by Putirka (2008) and Roeder and Emslie (1970).

3.1.2. Dissolution-crystallization experiment

The APR16-D1Ab run (1300 °C; 0.8 GPa; 2 h) exhibits textural features resulting from dissolution-crystallization processes. In particular, the large cpx Ves displays smoothed edges on which a 10-50 µm-thick layer (i.e., cpx Ves rim) overgrew (Fig. 6a, b, d). Notably, a precipitation layer with cellular texture overgrew on the cpx Ves rim along the lateral faces of the residual crystal (Fig. 6d). Moreover, new euhedral cpx crystals with size up to 200 µm formed towards the top of the capsule adjacent to the overgrown rim (Fig. 6a, c). Some of these new cpx, are zoned and, depending on the crystal size and zoning pattern, can be divided in two groups: group 1-new cpx are characterized by large crystals (~100 µm in size; Fig. 6a) formed by euhedral layer grown on anhedral cores (up to 30 µm in size), that probably represent restitic of natural starting material. Group 2-new cpx are characterized by small newly-growing cpx crystals (~20 µm in size; Fig. 6c) showing concentric oscillatory zoning with euhedral shape.

The overgrown rim is a diopside ($Wo_{49}En_{48}Fs_3$; Fig. 4) as for the residual cpx Ves, but with higher Mg# (0.93 vs. 0.89) and Al_2O_3 (4.88 wt.% vs. 1.53 wt.%) and lower SiO_2 (51.16 wt.% vs.

53.12 wt.%) contents. In the new zoned cpx crystals both cores and rims are still classified as diopside (Wo_{46}-En_{47}-Fs_{7} and Wo_{48}-En_{48}-Fs_{4}, respectively; Fig. 4) but their compositions are distinct from that of the residual cpx Ves. In particular, the cores of the group 1-new cpx have Mg# (0.88), SiO_2 (49.48 wt.%), and CaO (21.15 wt.%) lower than those of the rims (0.92, 51.21 wt.%, 23.13 wt.%, respectively) (Table S1 in Online Resource 3). Moreover, the crystal cores are enriched in TiO_2, Al_2O_3, FeO, Na_2O, and Cr_2O_3 (Table S1 in Online Resource 3). The group 2-new cpx are characterized by different oxide contents in relationship with the concentric oscillatory zonations (Fig. 6 and Table S1 in Online Resource 3). Their core composition falls in the augite field (Morimoto et al., 1998; Fig. 4) next to the boundary with diopside, while the mantle and the outer parts are both diopside. The gradual increase of CaO (from 20.6 to 22.6 wt. %) towards the crystal rim is counterbalanced by the decrease of FeO (from 3.7 to 2.6 wt.%). MgO clearly decreases from the core to the mantle (from ~17 to 15.5 wt.%) and then shows a limited change (MgO = ~16 wt.%) in the outermost portion (~10 mm far) of the grains, while the mantles of these new cpx are enriched in Al_2O_3, TiO_2, Na_2O_3, and Cr_2O_3 (Table S1 in Online Resource 3). Notably, the chemistry of the mantle of the group 2-new cpx and that of the cores of the group1-new cpx (i.e., restitic cpx phenocrysts of the APR16-starting material) compare well with the composition of the cpx crystallized at 0.8 GPa in equilibrium with the APR16 residual melt, as reported in Bonechi et al. (2020a) (Fig. 4; Table S1 in Online Resource 3). Finally, the composition of the large unzoned new cpx is diopsidic ($Wo_{49}En_{47}Fs_{4}$; Fig. 4) and closely approaches that of the cpx Ves rim and those of the crystal rims from group 1- and group 2-new cpx (Table S1 in Online Resource 3).

The chemical composition of the glass in this run is heterogeneous showing marked differences between the portion near the top of the capsule (hereafter identified as APR16-D1Ab) and that in the new-cpx zone (i.e., APR16-D1Ab*). Figure 5 shows that the composition of APR16-D1Ab

glass is in the trend outlined by the glasses of the dissolution experiments. Conversely, the APR16-D1Ab* glass shows lower SiO_2 (~46 wt.%), TiO_2 (~1 wt.%) and Al_2O_3 (~14 wt.%), as well as higher Mg# (0.79) and CaO (~18 wt.%) than those of the APR16-D1Ab glass (~50 wt.%, ~1.2 wt.%, 0.77, ~14 wt.%, respectively). Both glass compositions were used to calculate $K_D(Fe\text{-}Mg)^{cpx\text{-}liq}$ in order to identify the possible equilibrium condition among the different types of cpx crystallized during this experiment. Using the APR16-D1Ab glass, the obtained values are: 0.38±0.02 for the cpx Ves, 0.25±0.01 for the cpx Ves rim and for the unzoned, new cpx, 0.49±0.03 for the group 1-new cpx core, 0.28±0.01 for the group 1-new cpx rim, 0.40±0.02 for the group 2-new cpx core, 0.44±0.02 for the group 2-new cpx mantle, and 0.31±0.01 for the group 2-new cpx rim. Using the APR16-D1Ab* glass, the obtained values are: 0.44±0.03 for the cpx Ves, 0.29±0.01 for the cpx Ves rim and for the unzoned, new cpx, 0.56±0.04 for the group 1-new cpx core, 0.33±0.01 for the group 1-new cpx rim, 0.46±0.02 for the group 2-new cpx core, 0.51±0.03 for the group 2-new cpx mantle, and 0.35±0.01 for the group 2-new cpx rim. According to the equilibrium range of Putirka (2008), the cpx Ves and the new cpx cores are in disequilibrium with both APR16-D1Ab and APR16-D1Ab* melts, whereas the cpx Ves rim, the unzoned, new cpx, group 1- and group 2-new cpx rims are in equilibrium with APR16-D1Ab* composition.

3.2. Dissolution rates

Dissolution rates have been calculated by the difference between initial and final length of cpx Ves before and after the experiment (Δr) divided by the time duration of experimental run (e.g., Chen and Zhang, 2009). Data reported in Table 3 are $7.9 \cdot 10^{-6}$ cm s^{-1} for APR16-D1Aa (1350 °C; 0.8 GPa; 0.5 h) and $6.1 \cdot 10^{-6}$ cm s^{-1} for APR16-D1A (1350 °C; 0.8 GPa; 1 h).

For the APR16-D1Ab run (1300 °C; 0.8 GPa; 2 h), it was not possible to directly calculate the dissolution rate due to the effect of crystallization during the experiment. These dissolution rates are consistent with the convective dissolution rates (from 10^{-5} to 10^{-7} cm s^{-1}) obtained by Brearley and Scarfe (1986) at temperatures (1250-1500 °C), ΔT (25-125 °C), pressures (0.5-3 GPa) and dwell time (0.16-2 h) comparable with those employed in our experiments (Table S2 in Online Resource 3).

3.3. In situ observation of dissolution

In situ observation of the cpx dissolution in the melt allows to monitor morphological changes in real time, to determine any orientation effects as well as possible sinking (or floating) due to density contrast between crystal and melt. In this case the radiographic photomicrographs collected during the APR16-D1 run (1570 °C; 2 GPa) made possible to estimate the time taken by the cpx Ves to dissolve and the process through which it occurred. Importantly, quantitative understanding of the results are challenging because it requires the knowledge of the liquidus *T* of both cpx and glass at the *P*-*T* of interest. In addition, attention must be paid at possible incongruent melting or precipitation of Si-rich droplets during the early partial melting as reported by Raterron et al. (1995) that might affect the dissolution rate. For this reason, we decided to conduct this experiment at higher *P* compared to the experiments described above to allow increase of *T* (near the liquidus *T* of cpx Ves) and, in turn, speed up the dissolution. In particular, the collected frames allowed to quantify the change of the cpx dimensions as a function of time. Figure 7 shows that the crystal size decreases with increasing time, following a non-linear trend characterized by apparent slope increase at around 2.5 s, after which crystal dissolution proceeds until the complete disappearance of cpx crystal. It is interesting to note that

in correspondence of the increase of the slope (after 2.5 s) the crystal loses its euhedrality developing a sub-rounded morphology.

Due to this different behavior, we calculated average dissolution rates of $4.8 \cdot 10^{-3}$ cm s^{-1} up to 2.5 s and $3.2 \cdot 10^{-2}$ cm s^{-1} after 2.5 s.

4. Discussion

Photomicrographs of experimental runs show that cpx dissolution occurs by consumption of crystalline faces with the formation of subrounded shapes and/or indentations (Fig. S4 in Online Resource 1). Radiographic Movie from APR16-D1 run documents that the dissolution process develops by symmetric consumption of the crystalline faces. According to our experimental data, textural changes typical of patchy, sieve or spongy cpx phenocrysts that often characterize natural magmatic environments, may be the result not only of mineral dissolution but also of overgrowth processes (Perinelli et al., 2008; Tsuchiyama, 1986), as observed for example in natural plagioclase phenocrysts (e.g., Fornaciai et al., 2015; Viccaro et al., 2010). In the following paragraphs, in situ dissolution, dissolution, and dissolution-crystallization mechanisms are examined and discussed.

4.1. In situ dissolution experiment

As it can be seen in Figure 7, the dissolution process seems to be characterized by a faster crystal dissolution with increasing time. This could depend on the variation of the size of crystal during the dissolution. However, although small crystals (~0.2 mm of radius) dissolve slightly more rapidly than the larger ones (~0.6 mm of radius) during convective dissolution or melting (Zhang and Xu, 2003), the rate difference is not so large. During the in situ experiment a continuous increase in temperature was performed until no changes were detected through real-time

monitoring. Therefore, considering that the thermal diffusivity through the sample is ~10^{-6} m^2 s^{-1} (e.g., Zhang and Sun, 2017) and the distance of the crystal from the heating element is in the order of ~mm, the time required for thermal diffusion from the element to the crystal is on the order of the dissolution timescale (i.e., ~seconds). This suggests the occurrence of a transition from dissolution (above the liquidus of the glass but below the cpx solidus) to partial melting (between the solidus and liquidus of cpx) to melting of cpx (above the liquidus of cpx) as the sample is heated up. Particularly, the first stage of dissolution occurred when the experimental temperature on the sample was above the liquidus of the APR16GL (T_L ~1460 °C at 2 GPa; Table 2) and below the liquidus of the cpx crystal (i.e., T < 1597 °C; Table 2) while the second stage of really high dissolution rate occurred at temperature near/above the cpx liquidus temperature (i.e., $T \geq 1597$ °C). In this regard, since the nominal temperature of the experiment has an uncertainty of ~60 °C as reported by Kono et al. (2014b), it is probable that the actual temperature on the sample during the last seconds of the Movie 1 was close or a little higher than the T liquidus of the cpx Ves (i.e., ~1597 °C) causing the rapid and complete disappearance of the cpx crystal.

4.2. Dissolution experiments

Cpx dissolution rates from these experiments are comparatively combined with the convective dissolution data in Brearley and Scarfe (1986) and plotted in Fig. 8 as function of ΔT (a) and temperature (b). Among the data available in literature (e.g., Brearley and Scarfe, 1986; Chen and Zhang, 2009; Zhang et al., 1989; see Table S2 in Online Resource 3), we considered for the comparison only the dissolution rates of Brearley and Scarfe (1986) since they are time-independent convective dissolution rates like those of this study. Conversely, the dissolution rates by Chen and Zhang (2009) and Zhang et al. (1989) were not considered since they are time-

dependent diffusive dissolution rates and cannot be directly compared with time-independent convective dissolution rates using linear dissolution. As already demonstrated by previous authors (Brearley and Scarfe, 1986; Chen and Zhang, 2009; Van Orman and Grove, 2000; Zhang et al., 1989), temperature enhances not only the chemical diffusivity in the melt, but also the interfacial composition of the melt (which is correlated with ΔT). Both of these contribute to the dissolution rate by controlling the diffusional flux of the rate controlling component(s). In particular, the dissolution rate increases with increasing both ΔT (Fig. 8a) and T (Fig. 8b). Thus, we modelled the dissolution rate as function of T and ΔT by integrating data from this study with those of Brearley and Scarfe (1986) performed at P = 0.5-1 GPa and t = 600-3600 s (Table S2 in Online Resource 3), as reported in the following equation valid for ΔT >0 :

$$\text{Log Diss. rate} = 0.0048(\pm 0.0020) * T + 0.0046(\pm 0.0039) * \Delta T - 11.987(\pm 2.450) \quad (1),$$

with R^2 = 0.87 and SEE = 0.14 (where R is the correlation coefficient and SEE is the standard error of estimate; Fig. 8c). The multiple regression analysis showed a very good correlation between dissolution rate and T and ΔT. For comparable values of T and ΔT, we noted that pressure does not show any strong influence on the dissolution rate at P <2 GPa, as also previously observed for diffusive dissolution by Chen and Zhang (2009). At P >2 GPa, instead, the dissolution rate would seem to decrease with increasing pressure.

4.3. Dissolution-crystallization phenomena

APR16-D1Ab run is characterized by a dissolution-crystallization process due to a low APR16-powder/cpx Ves ratio (Table 2). As a consequence, $T_{liquidus}$ of the bulk composition (APR16+cpx Ves) increases to 1384 °C (ΔT = -84 °C; Table S3 in Online Resource 3), as estimated by

Rhyolite-MELTS software (Asimow and Ghiorso, 1998; Gualda et al., 2012). Textural and compositional data indicate that the crystallization process is preceded by a dissolution process (Fig. 6). Figure 9 and Table 4 show a step-by-step schematic model which reconstructs the process of early cpx Ves dissolution and late formation of new cpx crystals. At the beginning of the experiment (t_0), the system is formed by the cpx Ves and the APR16 starting material which contains some restitic natural phenocrysts. At t_1, the dissolution is triggered by the destabilization of the cpx Ves whose chemistry is in disequilibrium with that of K-basalt at 0.8 GPa (Perinelli et al. 2019). During cpx Ves dissolution, the diffusion of cations in the melt does not substantially change the far-field melt composition of APR16, from which new cpx crystal portions (i.e., the core and mantle of group 2-new cpx; Fig. 9) start to crystallize. Notably, both core and mantle of group 2-new cpx are in local equilibrium with APR16 melt as testified by the $K_D(Fe\text{-}Mg)^{cpx\text{-}liq}$ values (~0.25 for the core and ~0.27 for the mantle; Fig. S5 in Online Resource 1). At t_2, the diffusion of cations in the melt becomes more effective and the composition of APR16 melt progressively changes. Accordingly, the chemistry of newly-formed cpx crystals also changes, leading to the formation of a further type of cpx, either as single crystals (unzoned new cpx) or overgrowth rims (cpx Ves rim, group 1-new cpx and group 2-new cpx rims; Fig. 9). At t_3 (corresponding to the end of the experiment), the bulk system is composed of 1) partially resorbed cpx Ves characterized by a Ves rim, 2) new cpx crystals both oscillatory and inversely zoned, 3) unzoned new cpx crystals (Fig. 6), and 4) the inhomogeneous glass. The Mg# value of glass increases from 0.68 (APR16-Mg# value at t_0) to 0.79 near to the residual cpx Ves or to 0.77 at ~500 µm far from it (Table S1 in Online Resource 3). The glass results in equilibrium with the cpx Ves rim and the new cpx rims ($K_D(Fe\text{-}Mg)^{cpx\text{-}liq}$ = 0.29-0.35; Fig. S5 and Table S1 in Online Resource 1 and 3, respectively). The effective time lapse during which the dissolution operates (t_1 step, see above) is unknown. However, a rough time estimation can be provided by

using literature data on mineral dissolution rates determined at ΔT between 20 and 40 °C (Table S2 in Online Resource 3), and comparable to ΔT = 20 °C of APR16-D1Ab run. At these conditions, the dissolution rate covers a range of values of three orders of magnitude ($2.5 \cdot 10^{-5}$ and $1.4 \cdot 10^{-7}$ cm s^{-1}; Table S2 in Online Resource 3), and the time required to dissolve ~0.02 cm of cpx Ves (Fig. 9 and Table 3) varies from ~0.5 to ~1.4 h using dissolution rates (i.e., $1 \cdot 10^{-5}$ and $4 \cdot 10^{-6}$ cm s^{-1}) compatible with the experimental dwell time (i.e., 2 h; Table 2). Therefore, the crystallization of the cpx Ves and new cpx rims and unzoned new cpx crystals occurred in a maximum time of 1.44 h with a growth rate of ~$1.35 \cdot 10^{-6}$ cm s^{-1}. Noteworthy, this value is greater than those experimentally determined by Bonechi et al. (2020a) at the same pressure conditions and using APR16GL composition as starting material (e.g., ~10^{-7}-10^{-8} cm s^{-1} for dwell time in the range of 0.25-9 h). Conversely, it is comparable with the cpx growth rates (~$1 \cdot 10^{-6}$ cm s^{-1}) obtained from kinetic experiments performed at high cooling rates (i.e., ≥ 80 °C min^{-1}; Burkhard, 2002; Pontesilli et al., 2019) and high degrees of undercooling (i.e., the difference between the phase-in temperature of the melt and the quench temperature ΔT^* ≥ 80 °C; Burkhard, 2002; Pontesilli et al., 2019). This latter correspondence can be related to the compositional change of the APR16 melt caused by the dissolution of cpx Ves. The liquidus temperature of the melt increases from 1280 °C for APR16 to 1332 °C for APR16-D1Ab* (Table S3 in Online Resource 3). However, the limited variation of $T_{liquidus}$ indicates low-to-moderate undercooling conditions during steps t_2 and t_3 (maximum ΔT^* = 52 °C), with maintenance of low degrees of cpx supersaturation in the melt and high cation mobilities (Hammer, 2008 and reference therein). Despite high crystal growth rates are more commonly associated with high degrees of undercooling and development of anhedral to dendritic/skeletal crystal morphologies (e.g., Cashman, 1993; Conte et al., 2006; Hammer, 2008), these conditions were suitable for the

formation of euhedral, unzoned new cpx (up to ~200 mm in size) in chemical equilibrium with the APR16-D1Ab* melt (Fig. 9).

4.4. Implications to magma dynamics

Mineral dissolution and/or re-crystallization phenomena due to magma mixing, often produce phenocryst assemblages with disequilibrium textures and mineral zoning. In this context, intracrystalline cation exchange models are commonly used to calculate crystal residence times and magma ascent rates (e.g., Petrone et al., 2018; Viccaro et al., 2016) as well as the time elapsed between the refilling of a new and more mafic magma into sub-volcanic reservoirs and eruptions (e.g., Perugini et al., 2015; Rossi et al., 2019; Ubide and Kamber, 2018). Only sporadic studies have also considered the role played by crystal dissolution phenomena during crystal-melt interaction and crystal growth (e.g., Liang 2003). If magma mixing is accompanied by crystal dissolution, then it is likely that most of retrieved residence times are potentially underestimated. The refilling of sub-volcanic reservoirs by a new magma batch is proposed as one of the major processes capable of triggering explosive volcanic eruptions due to abrupt changes of the intensive-extensive variables of the system (e.g., Nakamura, 1977; Sparks et al., 1977; Viccaro et al., 2006). Understanding the timing of volcanic eruptions is a central issue, particularly to densely populated, active volcanic settings, such as Campi Flegrei caldera (Southern Italy). Many authors identified in the eruptive products of Campi Flegrei several textural and compositional features that can be traced back to mingling-mixing processes (e.g., Arienzo et al., 2010; D'Antonio et al., 2007; Di Renzo et al., 2011; Orsi et al., 1995). Through basalt-phonolite mixing experiments, it has been suggested that the time-scales of mixing for some recent eruptions (namely, Astroni, Averno and Agnano Monte Spina) is in the order of tens of minutes (Perugini et al., 2015). We are aware that *P-T* conditions investigated in this

study are quite different from those encountered at shallow crustal depths where magma mixing takes place (e.g., Arienzo et al., 2010; D'Antonio et al., 2007; Di Renzo et al., 2011; Orsi et al., 1995). However, our experimental data may be combined with the textural information gained by using natural cpx phenocrysts from the pyroclastic deposits of Agnano-Monte Spina eruption (4100 BP; de Vita et al., 1999) to obtain a rough estimation for the crystal dissolution time. This approach may be reasonable considering that *i*) the pressure has negligible influence on the dissolution rate (see in the above § 4.2.2. section), and *ii*) the investigated *T* range is high (1300-1350 °C), and *iii*) the temperature of basaltic magmas intruding into the shallow reservoirs is high too (*T* >1150 °C; Fowler et al., 2007). This comparatively approach provides a preliminary evaluation for the effect of crystal dissolution on mixing time scales, by calculating the dissolution time of cpx phenocrysts whose morphological and chemical features testify to magma mixing processes (Fig. 10). The selected zoned crystals were separated from trachytic crystal-rich pumice (Forni et al., 2016, 2018). The mineral composition is diopsidic with maximum values of Mg# (80-89) restricted to the crystal portions with shapes suggesting crystal-resorption events (dark gray areas in BSE photomicrographs showed in Fig. 10). These Mg#-rich crystal portions are relicts of early-formed cpx phenocrysts (hereafter named AMS-Cpx1) from a more primitive magmas rising from greater depths (depths ≥ 8 km; Arienzo et al. 2010 and references therein) and mixing with the resident evolved magma. Among selected zoned crystals, relict crystals show maximum and minimum sizes in the order of ~1 mm and ~150 μm, respectively. According to the dissolution rates of ~10^{-5}-10^{-6} cm s^{-1} experimentally derived for the basaltic end-member of Campi Flegrei caldera (i.e., APR16 sample), the minimum dissolution time for a resorption of 150 μm ranges from ~25 min to ~4 h. This time interval is slightly higher than the time scales of mixing of 15±4, 18±5, and 13±4 min proposed by Perugini et al. (2015) for Agnano-Monte Spina, Averno, and Astroni eruptions, respectively. It is not

possible to know if magma mixing caused the partial or complete dissolution of larger AMS-cpx1 phenocrysts. For this reason, we have considered for the calculation a maximum length that corresponds to largest AMS-Cpx1 (0.15 cm; Fig. 10a). This phenocryst results to be less affected by dissolution. The time required for partial (ΔL ~0.08 cm where ΔL is the difference between the initial and the final crystal length) or complete resorption (ΔL ~0.15 cm) of AMS-cpx1 varies from at least ~2 to ~23 h or from ~4 to ~39 h, by assuming dissolution rates of ~10^{-5} cm·s^{-1} and ~10^{-6} cm s^{-1}, respectively.

5. Conclusions

In this experimental work, we have determined the dissolution rate of cpx interacting with a K-basalt at high pressure. Values calculated at pressure of 0.8 GPa, temperature of 1350 °C, and dwell times between 0.5 and 1 h are in the order of ~10^{-5}-10^{-6} cm s^{-1}. By the in situ experiment at 2 GPa and ~1570 °C, we have evaluated the cpx dissolution rate at temperatures above the liquidus temperature of glass and near the liquidus temperature of cpx (T_{cpxL}), showing a non-linear trend over time, with apparent acceleration when temperatures near/above the melting point of the cpx are reached (~1597 °C). Specifically, the assessed dissolution rate increases from $4.8 \cdot 10^{-3}$ cm s^{-1} for temperature conditions below the T_{cpxL} to $3.2 \cdot 10^{-2}$ cm s^{-1} for temperatures near/above the T_{cpxL}. The increase of dissolution rate is accompanied by a textural evolution of the cpx which passes from crystalline faces in the first seconds to a sub-rounded shape until it disappears completely at the end of the experiment. This along with textural features of the quenched 0.8 GPa runs indicate that the dissolution process occurs by consumption of crystalline faces independently of the crystal orientation, leading to rounded shapes and indentations. In the dissolution-crystallization experiment, the formation of overgrowth rims and new cpx crystals with different textures and compositions suggests that injection of basaltic melts in a cold magma

chamber may produce crystals with inverse or oscillatory zonation. This disequilibrium crystallization process is also related to the dissolution of pristine crystals resident in the magma reservoir. The growth rate ($1.35 \cdot 10^{-6}$ cm s^{-1}) extrapolated from this dissolution-crystallization experiment, confirms that dynamic conditions favor rapid crystal growth rates. By applying the experimental dissolution rates calculated in this study to products of Agnano-Monte Spina eruption (4100 BP) at Campi Flegrei caldera (Campanian region, Italy), we have estimated maximum cpx dissolution time-scale of ~40 h.

Acknowledgment

We warmly thank the reviewers J. Van Orman and Y. Zhang and the Editor D. Dingwell for their very helpful, constructive and resolutive comments. We thank Luca Ziberna (BGI Bayreuth) for preparing APR16GL sample. We thank D. Mannetta (Dipartimento Scienze della Terra, Sapienza Università di Roma) for his help in preparing the cpx Ves, M. Albano (CNR-IGAG), Dr. R. Jedlicka (Institute of Petrology and Structural Geology, Charles University of Prague) and M. Serracino (CNR-IGAG) for assistance during SEM and EPMA analytical sessions. We thank Dr. M. Racek (Institute of Petrology and Structural Geology, Charles University of Prague) for his help in performing and processing crystal orientation data analysis.

Funding

This research has been conducted with the financial support of the HP-HT Laboratory at the Department of Earth Sciences of Sapienza - University of Rome and with the financial support of the project M_011177_14_D_MAGRI_10-MIUR funded to B.B. The experiment with PE was performed at HPCAT (Sector 16), Advanced Photon Source (APS), Argonne National Laboratory. HPCAT operations are supported by DOE-NNSA's Office of Experimental

Sciences. The Advanced Photon Source is a U.S. Department of Energy (DOE) Office of Science User Facility operated for the DOE Office of Science by Argonne National Laboratory under Contract No. DE-AC02-06CH11357. V.S. acknowledges financial support from the DeepCarbon Observatory and Fondi di Ateneo Sapienza (2016).

Conflicts of interest/Competing interests

The authors declare that they have no known competing financial interests or personal relationships that could have appeared to influence the work reported in this paper.

Availability of data and material

Data will be made available on request.

References

Arienzo, I., Moretti, R., Civetta, L., Orsi, G., Papale, P., 2010. The feeding system of Agnano-Monte Spina eruption (Campi Flegrei, Italy): Dragging the past into present activity and future scenarios. Chem. Geol. 270, 135-147. https://doi.org/10.1016/j.chemgeo.2009.11.012

Asimow, P., Ghiorso, M.S., 1998. Algorithmic modifications extending MELTS to calculate subsolidus phase relations. Am. Mineral. 83, 1127–1132. https://doi.org/10.2138/am-1998-9-1022

Bonechi B., 2020. Influence of Pre-Existing Nuclei on the Crystallization Kinetics of Primitive Alkaline Magmas: Insights on the Deep Feeding System of the Campi Flegrei Volcanic District. Minerals 10, 234. https://doi:10.3390/min10030234

598 Bonechi, B., Perinelli, C., Gaeta, M., 2020a. Clinopyroxene growth rates at high pressure:
599 constraints on magma recharge of the deep reservoir of the Campi Flegrei Volcanic District
600 (south Italy). Bull. Volcanol. 82, 5. https://doi.org/10.1007/s00445-019-1342-5
601 Bonechi B., Perinelli C., Gaeta M., Tecchiato V. and Fabbrizio A., 2020b. Amphibole growth
602 from a primitive alkaline basalt at 0.8 GPa: Time-dependent compositional evolution,
603 growth rate and competition with clinopyroxene. Lithos 354–355, 105272.
604 https://doi.org/10.1016/j.lithos.2019.105272
605 Boyd, F.R., England, J.L., 1960. Apparatus for phase-equilibrium measurements at pressures up
606 to 50 kilobars and temperatures up to 1750 °C. J. Geophys. Res. 65, 741.
607 https://doi.org/10.1029/JZ065i002p00741
608 Brearley, M., Scarfe, C.M., 1986. Dissolution rates of upper mantle minerals in an alkali basalt
609 melt at high pressure: An experimental study and implications for ultramafic xenolith
610 survival. J. Petrol. 27, 1157–1182. https://doi.org/10.1093/petrology/27.5.1157
611 Burkhard, D.J., 2002. Kinetics of crystallization: Example of micro-crystallization in basalt lava.
612 Contrib. Mineral. Petrol. 142, 724–737. https://doi.org/10.1007/s00410-001-0321-x
613 Cashman, K. V, 1993. Relationship between plagioclase crystallization and cooling rate in
614 basaltic melts. Contrib. Mineral. Petrol. 113, 126-142. https://doi.org/10.1007/BF00320836
615 Chen, Y., Zhang, Y., 2008. Olivine dissolution in basaltic melt. Geochim. Cosmochim. Acta 72,
616 4756–4777. https://doi:10.1016/j.gca.2008.07.014
617 Chen, Y., Zhang, Y., 2009. Clinopyroxene dissolution in basaltic melt. Geochim. Cosmochim.
618 Acta 73, 5730–5747. https://doi.org/10.1016/j.gca.2009.06.016
619 Conte, A.M., Perinelli, C., Trigila, R., 2006. Cooling kinetics experiments on different Stromboli
620 lavas: Effects on crystal morphologies and phases composition. J. Volcanol. Geotherm. Res.
621 155, 179–200. https://doi.org/10.1016/j.jvolgeores.2006.03.025

D'Antonio, M., Civetta, L., Di Girolamo, P., 1999. Mantle source heterogeneity in the Campanian Region (South Italy) as inferred from geochemical and isotopic features of mafic volcanic rocks with shoshonitic affinity. Mineral. Petrol. 67, 163–192. https://doi.org/10.1007/BF01161520

D'Antonio, M., Tonarini, S., Arienzo, I., Civetta, L., Di Renzo, V., 2007. Components and processes in the magma genesis of the Phlegrean Volcanic District, southern Italy. Geol. Soc. Am. Spec. Pap. 418, 203–220. https://doi.org/10.1130/2007.2418(10).

De Astis, G., Pappalardo, L., Piochi, M., 2004. Procida volcanic history: New insights into the evolution of the Phlegraean Volcanic District (Campania region, Italy). Bull. Volcanol. 66, 622–641. https://doi.org/10.1007/s00445-004-0345-y

de Vita, S., Orsi, G., Civetta, L., Carandente, A., D'Antonio, M., Deino, A., di Cesare, T., Di Vito, M.., Fisher, R.., Isaia, R., Marotta, E., Necco, A., Ort, M., Pappalardo, L., Piochi, M., Southon, J., 1999. The Agnano–Monte Spina eruption (4100 years BP) in the restless Campi Flegrei caldera (Italy). J. Volcanol. Geotherm. Res. 91, 269–301. https://doi.org/10.1016/S0377-0273(99)00039-6

Di Renzo, V., Arienzo, I., Civetta, L., D'Antonio, M., Tonarini, S., Di Vito, M.A., Orsi, G., 2011. The magmatic feeding system of the Campi Flegrei caldera: Architecture and temporal evolution. Chem. Geol. 281, 227–241. https://doi.org/10.1016/j.chemgeo.2010.12.010

Donaldson, C.H., 1985. The Rates of Dissolution of Olivine, Plagioclase, and Quartz in a Basalt Melt. Mineral. Mag. 49, 683–693. https://doi.org/10.1180/minmag.1985.049.354.07

Edwards, B.R., Russell, J.K., 1998. Time scales of magmatic processes: New insights from dynamic models for magmatic assimilation. Geology 26, 1103–1106. https://doi.org/10.1130/0091-7613

Finnila, A.B., Hess, P.C., Rutherford, M.J., 1994. Assimilation by lunar mare basalts: melting of

crustal material and dissolution of anorthite. J. Geophys. Res. 99, 14677–14690. https://doi.org/10.1029/94je01380

Fornaciai, A., Perinelli, C., Armienti, P., Favalli, M., 2015. Crystal size distributions of plagioclase in lavas from the July–August 2001 Mount Etna eruption. Bull. Volcanol. 77, 70. https://doi.org/10.1007/s00445-015-0953-8

Forni, F., Bachmann, O., Mollo, S., De Astis, G., Gelman, S. E., Ellis, B.S., 2016. The origin of a zoned ignimbrite: Insights into the Campanian Ignimbrite magma chamber (Campi Flegrei, Italy). Earth Planet. Sci. Lett. 449, 259-271. https://doi.org/10.1016/j.epsl.2016.06.003

Forni, F., Degruyter, W., Bachmann, O., De Astis, G., Mollo, S., 2018. Long-term magmatic evolution reveals the beginning of a new caldera cycle at Campi Flegrei. Sci. Adv. 4(11), eaat9401. https://doi.org/10.1126/sciadv.aat9401

Fowler, S.J., Spera, F.J., Bohrson, W.A., Belkin, H.E., De Vivo, B., 2007. Phase equilibria constraints on the chemical and physical evolution of the campanian ignimbrite. J. Petrol. 48, 459–493. https://doi.org/10.1093/petrology/egl068

Ghiorso, M.S., Sack, R.O., 1995. Chemical mass transfer in magmatic processes IV. A revised and internally consistent thermodynamic model for the interpolation and extrapolation of liquid-solid equilibria in magmatic systems at elevated temperatures and pressures. Contrib. Mineral. Petrol. 119, 197–212. https://doi.org/10.1007/BF00307281

Gualda, G.A.R., Ghiorso, M.S., Lemons, R. V., Carley, T.L., 2012. Rhyolite-MELTS: A modified calibration of MELTS optimized for silica-rich, fluid-bearing magmatic systems. J. Petrol. 53, 875–890. https://doi.org/10.1093/petrology/egr080

Hammer, J.E., 2008. Experimental Studies of the Kinetics and Energetics of Magma Crystallization. Rev. Mineral. Geochemistry 69, 9–59.

https://doi.org/10.2138/rmg.2008.69.2

Johannes, W., Bell, P.M., Mao, H.K., Boettcher, A.L., Chipman, D.W., Hays, J.F., Newton, R.C., Seifert, F., 1971. An interlaboratory comparison of piston-cylinder pressure calibration using the albite-breakdown reaction. Contrib. Mineral. Petrol. 32, 24-38. https://doi.org/10.1007/BF00372231

Kelemen, P.B., 1990. Reaction between ultramafic rock and fractionating basaltic magma I. Phase relations, the origin of calc-alkaline magma series, and the formation of discordant dunite. J. Petrol. 31, 51–98. https://doi.org/10.1093/petrology/31.1.51

Kerr, R.C., 1995. Convective crystal dissolution. Contrib. Mineral. Petrol. 121, 237–246. https://doi.org/10.1007/BF02688239

Kirkpatrick, R. J., Robinson, G. R., Hays, J. F., 1976. Kinetics of crystal growth from silicate melts: anorthite and diopside. J. Geophys. Res., 81(32), 5715-5720. https://doi.org/10.1029/JB081i032p05715

Kono, Y., Irifune, T., Higo, Y., Inoue, T., Barnhoorn, A., 2010. P-V-T relation of MgO derived by simultaneous elastic wave velocity and in situ X-ray measurements: A new pressure scale for the mantle transition region. Phys. Earth Planet. Inter. 183, 196–211. https://doi.org/10.1016/j.pepi.2010.03.010

Kono, Y., Park, C., Kenney-Benson, C., Shen, G., Wang, Y., 2014a. Toward comprehensive studies of liquids at high pressures and high temperatures: Combined structure, elastic wave velocity, and viscosity measurements in the Paris-Edinburgh cell. Phys. Earth Planet. Inter. 228, 269–280. https://doi.org/10.1016/j.pepi.2013.09.006

Kono, Y., Kenney- Benson, C., Hummer, D., Ohfuji, H., Park, C., Shen, G., et al. 2014b. Ultralow viscosity of carbonate melts at high pressures. *Nat. Commun.*, *5*, 5091. https://doi.org/10.1038/ncomms6091

694 Kress, V.C., Ghiorso, M.S., 1995. Multicomponent diffusion in basaltic melts. Geochim.
695 Cosmochim. Acta 59, 313–324. https://doi.org/10.1016/0016-7037(94)00286-U
696 Kuo, L.C., Kirkpatrick, R.J., 1985a. Dissolution of mafic minerals and its implications for the
697 ascent velocities of peridotite-bearing basaltic magmas. J. Geol. 93, 691–700.
698 https://doi.org/10.1086/628996
699 Kuo, L.C., Kirkpatrick, R.J., 1985b. Kinetics of crystal dissolution in the system: diopside-
700 forsterite-silica. Am. J. Sci. 285, 51–90. https://doi.org/10.2475/ajs.285.1.51
701 Kutolin, V.A., Agafonov, L. V., 1978. Composition of the upper mantle in light of the relative
702 stability of ultramafic nodules. Geol. Geofiz. 19, 3–13.
703 Liang, L.H., Zhao, M., Jiang, Q., 2002. Melting enthalpy depression of nanocrystals based on
704 surface effect. J. Mater. Sci. Lett. 103, 239–248. https://doi.org/10.1023/A
705 Liang, Y., 2003. Kinetics of crystal-melt reaction in partially molten silicates: 1. Grain scale
706 processes. Geochem. Geophys. Geosyst. 4, 1045. https://doi.org/10.1029/2002GC000375
707 Liang, Y., 2000. Dissolution in molten silicates: Effects of solid solution. Geochim. Cosmochim.
708 Acta 64, 1617–1627. https://doi.org/10.1016/S0016-7037(00)00331-8
709 Liang, Y., 1999. Diffusive dissolution in ternary systems: Analysis with applications to quartz
710 and quartzite dissolution in molten silicates. Geochim. Cosmochim. Acta 63, 3983–3995.
711 https://doi.org/10.1016/s0016-7037(99)00203-3
712 Morabito, S., Petrosino, P., Milia, A., Sprovieri, M., Tamburrino, S., 2014. A multidisciplinary
713 approach for reconstructing the stratigraphic framework of the last 40 ka in a bathyal area
714 of the eastern Tyrrhenian Sea. Glob. Planet. Change 123, 121–138.
715 https://doi.org/10.1016/J.GLOPLACHA.2014.10.005
716 Morgan, D.J., Blake, S., Rogers, N.W., DeVivo, B., Rolandi, G., Macdonald, R., Hawkesworth,
717 C.J., 2004. Time scales of crystal residence and magma chamber volume from modelling

718 of diffusion profiles in phenocrysts: Vesuvius 1944. Earth Planet. Sci. Lett. 222, 933–946.
719 https://doi.org/10.1016/j.epsl.2004.03.030
720 Morgan, Z., Liang, Y., 2003. An experimental and numerical study of the kinetics of harzburgite
721 reactive dissolution with applications to dunite dike formation. Earth Planet. Sci. Lett. 214,
722 59–74. https://doi.org/10.1016/S0012-821X(03)00375-3
723 Morgan, Z., Liang, Y., Hess, P., 2006. An experimental study of anorthosite dissolution in lunar
724 picritic magmas: Implications for crustal assimilation processes. Geochim. Cosmochim.
725 Acta 70, 3477–3491. https://doi.org/10.1016/j.gca.2006.04.027
726 Morimoto, N., Fabries, J., Ferguson, A.K., Ginzburg, I.V., Ross, M., Seifert, F.A., J., Z., Aoki,
727 K., Gottardi, G., 1998. Nomenclature of pyroxenes Subcommittee. Am. Mineral. 73, 1123–
728 1133.
729 Nakamura, M., 1977. Continuous mixing of crystal mush and replenished magma in the ongoing
730 Unzen eruption. Geology 23, 807–810. https://doi.org/10.1130/0091-
731 7613(1995)023<0807:CMOCMA>2.3.CO;2
732 Navon, O., Stolper, E., 1987. Geochemical Consequences of Melt Percolation: The Upper
733 Mantle as a Chromatographic Column. J. Geol. 95, 285–307.
734 https://doi.org/10.1086/629131
735 Orsi, G., Civetta, L., D'Antonio, M., Di Girolamo, P., Piochi, M., 1995. Step-filling and
736 development of a three-layer magma chamber: the Neapolitan Yellow Tuff case history. J.
737 Volcanol. Geotherm. Res. 67, 291–312. https://doi.org/10.1016/0377-0273(94)00119-2
738 Perinelli, C., Gaeta, M., Bonechi, B., Granati, S.F., Freda, C., D'Antonio, M., Stagno, V., Sicola,
739 S., Romano, C., 2019. Effect of water on the phase relations of primitive K-basalts:
740 Implications for high-pressure differentiation in the Phlegraean Volcanic District magmatic
741 system. Lithos 342–343, 530–541. https://doi.org/10.1016/j.lithos.2019.05.032

742 Perinelli, C., Orlando, A., Conte, A.M., Armienti, P., Borrini, D., Faccini, B., Misiti, V., 2008.
743 Metasomatism induced by alkaline magma in the upper mantle of northern Victoria Land
744 (Antarctica): an experimental approach. Geol. Soc. London, Spec. Publ. 293, 279–302.
745 https://doi.org/10.1144/SP293.13
746 Perugini, D., De Campos, C.P., Petrelli, M., Dingwell, D.B., 2015. Concentration variance decay
747 during magma mixing: A volcanic chronometer. Sci. Rep. 5, 1–10.
748 https://doi.org/10.1038/srep14225
749 Petrone, C.M., Braschi, E., Francalanci, L., Casalini, M., Tommasini, S., 2018. Rapid mixing
750 and short storage timescale in the magma dynamics of a steady-state volcano. Earth Planet.
751 Sci. Lett. 492, 206–221. https://doi.org/10.1016/j.epsl.2018.03.055
752 Pontesilli, A., Masotta, M., Nazzari, M., Mollo, S., Armienti, P., Scarlato, P., Brenna, M., 2019.
753 Crystallization kinetics of clinopyroxene and titanomagnetite growing from a trachybasaltic
754 melt: New insights from isothermal time-series experiments. Chem. Geol. 510, 113–129.
755 https://doi.org/10.1016/j.chemgeo.2019.02.015
756 Presnall, D.C., Dixon, S.A., Dixon, J.R., O'Donnell, T.H., Brenner, N.L., Schrock, R.L., Dycus,
757 D.W., 1978. Liquidus phase relations on the join diopside-forsterite-anorthite from 1 atm
758 to 20 kbar: Their bearing on the generation and crystallization of basaltic magma. Contrib.
759 Mineral. Petrol. 66, 203–220. https://doi.org/10.1007/BF00372159
760 Putirka, K.D., 2008. Thermometers and Barometers for Volcanic Systems, in: Putirka, K.D.,
761 Tepley III, F.J. (Eds.), Minerals, Inclusions And Volcanic Processes. Reviews in
762 Mineralogy and Geochemistry, pp. 61–120. https://doi.org/10.2138/rmg.2008.69.3
763 Raterron, P., Bussod, G.Y., Doukhan, N., & Doukhan, J.C., 1997. Early partial melting in the
764 upper mantle: an AEM study of a lherzolite experimentally annealed at hypersolidus
765 conditions. Tectonophysics, 279, 79-91. https://doi.org/10.1016/S0040-1951(97)00131-5.

766 Reiners, P.W., 1998. Reactive melt transport in the mantle and geochemical signatures of mantle-
767 derived magmas. J. Petrol. 39, 1039–1061.
768 Roeder, P.L., Emslie, R.F., 1970. Olivine-liquid equilibrium. Contrib. Mineral. Petrol. 29, 275–
769 289. https://doi.org/10.1007/BF00371276
770 Rossi, S., Petrelli, M., Morgavi, D., Vetere, F.P., Almeev, R.R., Astbury, R.L., Perugini, D.,
771 2019. Role of magma mixing in the pre-eruptive dynamics of the Aeolian Islands volcanoes
772 (Southern Tyrrhenian Sea, Italy). Lithos 324–325, 165–179.
773 https://doi.org/10.1016/j.lithos.2018.11.004
774 Scarfe, C.M., Takahashi, E., Yoder Jr., H.S., 1980. Rates of dissolution of upper mantle minerals
775 in an alkali-olivine basalt melt at high pressure, in: Carnegie Inst. Washington Yearbook.
776 pp. 290–296.
777 Shaw, C.S.J., 2006. Effects of melt viscosity and silica activity on the rate and mechanism of
778 quartz dissolution in melts of the CMAS and CAS systems. Contrib. Mineral. Petrol. 151,
779 665–680. https://doi.org/10.1007/s00410-006-0086-3
780 Shaw, C.S.J., 2000. The effect of experiment geometry on the mechanism and rate of dissolution
781 of quartz in basanite at 0.5 GPa and 1350 °C. Contrib. Mineral. Petrol. 139, 509–525.
782 https://doi.org/10.1007/s004100000153
783 Sparks, S., Sigurdsson, H., Wilson, L., 1977. Magma mixing: a mechanism for triggering acid
784 explosive eruptions. Nature 267, 315–318. https://doi.org/10.1038/267315a0
785 Tsuchiyama, A., 1986. Melting and dissolution kinetics: application to partial melting and
786 dissolution of xenoliths. J. Geophys. Res. 91, 9395–
787 9406. https://doi.org/10.1029/JB091iB09p09395
788 Tursack, E., Liang, Y., 2012. A comparative study of melt-rock reactions in the mantle:
789 Laboratory dissolution experiments and geological field observations. Contrib. Mineral.

790 Petrol. 163, 861–876. https://doi.org/10.1007/s00410-011-0703-7
791 Ubide, T., Kamber, B.S., 2018. Volcanic crystals as time capsules of eruption history. Nat.
792 Commun. https://doi.org/10.1038/s41467-017-02274-w
793 Van Orman, J.A., Grove, T.L., 2000. Origin of lunar high- titanium ultramafic glasses:
794 Constraints from phase relations and dissolution kinetics of clinopyroxene- ilmenite
795 cumulates. Meteorit. Planet. Sci. 35, 783–794. https://doi.org/10.1111/j.1945-
796 5100.2000.tb01462.x
797 Viccaro, M., Barca, D., Bohrson, W., D'Oriano, C., Giuffrida, M., Nicotra, E., Bradley, W.,
798 Pitcher, B.W., 2016. Crystal residence times from trace element zoning in plagioclase reveal
799 changes in magma transfer dynamics at Mt. Etna during the last 400 years. Lithos 248–251,
800 309–323. https://doi.org/10.1016/j.lithos.2016.02.004
801 Viccaro, M., Ferlito, C., Cortesogno, L., Cristofolini, R., Gaggero, L., 2006. Magma mixing
802 during the 2001 event at Mount Etna (Italy): effects on the eruptive dynamics. J. Volcanol.
803 Geotherm. Res. 149, 139–159. https://doi.org/10.1016/j.jvolgeores.2005.06.004
804 Viccaro, M., Giacomoni, P., Ferlito, C., Lithos, R.C.-, 2010, U., 2010. Dynamics of magma
805 supply at Mt. Etna volcano (Southern Italy) as revealed by textural and compositional
806 features of plagioclase phenocrysts. Lithos 116, 77–91.
807 https://doi.org/10.1016/j.lithos.2009.12.012
808 Watson, E.B., 1982. Basalt contamination by continental crust: Some experiments and models.
809 Contrib. Mineral. Petrol. 80, 73–87. https://doi.org/10.1007/BF00376736
810 Williams, D.W., Kennedy, G.C., 1969. Melting curve of diopside to 50 kilobars. J. Geophys.
811 Res. 74, 4359–4366. https://doi.org/10.1029/JB074i017p04359
812 Yoder, H.S., 1952. Change of Melting Point of Diopside with Pressure. J. Geol. 60, 364–374.
813 https://doi.org/10.1086/625984

Yu, Y., Zhang, Y., Chen, Y., Xu, Z., 2016. Kinetics of anorthite dissolution in basaltic melt. Geochim. Cosmochim. Acta 179, 257–274. https://doi.org/10.1016/j.gca.2016.02.002

Zhang, Y., 2008. Geochemical kinetics. Princeton University Press.

Zhang, Y., Walker, D., Lesher, C.E., 1989. Diffusive crystal dissolution. Contrib. Mineral. Petrol. 102, 492–513. https://doi.org/10.1007/BF00371090

Zhang, Y. and Sun, Q., 2017. Temperature and pressure effects on basalt thermal diffusivity – a review. Geotech. Lett. 7, 315–322, http://dx.doi.org/10.1680/jgele.17.00064

Zhang, Y. and Xu, Z., 2003. Kinetics of convective crystal dissolution and melting, with applications to methane hydrate dissolution and dissociation in seawater. Earth Planet. Sci. Lett. 213, 133–148. https://doi.org/10.1016/S0012-821X(03)00297-8

Figure caption

Figure 1 *T* and *P* conditions of cpx dissolution experiments. Data sources: black cross this study (49 wt.% SiO_2); star Scarfe et al. (1980), convective cpx dissolution in alkali basalt (47 wt.% SiO_2); triangle Brearley and Scarfe (1986), cpx dissolution in alkali basalt (49 wt.% SiO_2); diamond Zhang et al. (1989), diffusive diopside dissolution in andesite (56.3 wt.% SiO_2); square Van Orman and Grove (2000), diffusive diopside dissolution in lunar ferrobasalt (47 wt.% SiO_2); circle Chen and Zhang (2009) (51.2 wt.% SiO_2). Colours indicate pressure ranges: green 0.5 GPa, yellow 1 GPa, orange 1.2 GPa, red 1.3 GPa, brown 1.4 GPa, light blue 2 GPa, blue 2.2 GPa, dark blue 3 GPa. The solid red curve is the pure diopside melting curve by Boyd and England (1963), Williams and Kennedy (1969) and Yoder (1952). The dashed green curve is the Vesuvius cpx melting curve while the dashed black curve is the rough liquidus of the alkaline basalt used in this study, both estimated by MELTS program (Asimow and Ghiorso, 1998; Ghiorso and Sack, 1995).

838 **Figure 2** Backscattered image of APR16-D1Aa run. Polished cpx Ves is indicated in green.
839 Inside the cpx Ves the crystallographic axes are reported (a in red, b in green, c in blue) following
840 the orientations showed by the upper-hemisphere projections (inset in the upper side of the
841 figure). As possible to see from these projections the polished surface is approximately
842 perpendicular to the c-axis (001). In the figure the profiles along which we measured the
843 variation of the major elements concentration in the melt are indicated with different coloured
844 lines: D1Aa_T1 in yellow, D1Aa_T2 in light blue, and D1Aa_T3 in green. An example is
845 reported in the insets on the right, where the concentration profiles of MgO and CaO are shown.
846 Finally, in the lower left part of the figure is reported a cartoon showing the sizes, the placement,
847 and the orientation of the cpx Ves before and after the experiment. The table reports the initial
848 (i) sizes, the final (f) sizes and the difference between them (Δr). Cartoon not in scale.
849 **Figure 3** Backscattered image of APR16-D1A run. Polished cpx Ves is indicated in green. Inside
850 the cpx Ves the crystallographic axes are reported (a in red, b in green, c in blue) following the
851 orientations showed by the upper-hemisphere projections (inset in the upper side of the figure).
852 As possible to see from these projections the polished surface is approximately perpendicular to
853 the b-axis (010). In the figure the profiles along which we measured the variation of the major
854 elements concentration in the melt are indicated with different coloured lines: D1Aa_T1 in teal
855 colour, D1Aa_T2 in yellow. An example is reported in the insets on the right, where the
856 concentration profiles of MgO and CaO are shown. Finally, in the lower left part of the figure is
857 reported a cartoon showing the sizes, the placement, and the orientation of the cpx Ves before
858 and after the experiment. The table reports the initial (i) sizes, the final (f) sizes and the difference
859 between them (Δr). Cartoon not in scale.
860 **Figure 4** Clinopyroxene compositions plotted into a magnification of the pyroxene classification
861 diagram (Morimoto et al., 1998). Wo: wollastonite; En: enstatite; Fe: ferrosilite; Di: diopside,

He: hedenbergite. The inset shows the whole diagram. Cross indicates the Vesuvius cpx, diamonds the residual cpx Ves, squares the group 1-new cpx and circles the group 2-new cpx. Empty symbols indicate cpx core, while filled symbols indicate cpx rim. For group-2-new cpx the lighter filled symbols indicate the mantle while the darker filled symbols the rim. New cpx unzoned of D1Ab run is not reported since its composition matches that of the cpx Ves rim. Yellow field shows cpx composition from Bonechi et al. (2020a).

Figure 5 Variation diagrams of major element with Mg# for residual glasses far from the residual cpx Ves. Cross indicates the starting material (SM) and circles the compositions of synthetic glasses. Error bars not reported are within the symbols size.

Figure 6 Backscattered photomicrographs of the APR16-D1Ab run. Insights show a-c) the top, b) the bottom and d) the side of the capsule. Cpx, clinopyroxene, Rim, reaction rim between cpx Ves and glass.

Figure 7 X-ray radiography frames of dissolution of cpx Ves (in green) in APR16GL melt at 2 GPa and ~1570 °C. Scale bar 0.2 mm. The diagram reports the variation of the crystal sizes *L* (light green circles), *W* (dark green circles) and their mean value (*M*; grey circles) with time for each frame (0.5 s interval).

Figure 8 Dissolution rate diagrams as function of a) ΔT (°C) and b) temperature (°C). Literature data from Brearley and Scarfe (1986). Pressure values of the reported experiments are between 0.5 and 3 GPa while time values vary between 500 and 7200 s. c) The accuracy of the Eq. 1 in the estimation of the dissolution rate as function of T and ΔT has been tested by comparing convective dissolution rate observed and the values predicted by the Equation 1 for the experiments of this study and for those of Brearley and Scarfe (1986). Among these latter, only data with conditions of P (0.5-1 GPa) and time (600-3600 s) similar to the experimental

conditions of our study are reported in this diagram (Table S2 in Online Resource 3). Symbols are as in Figure 1. Error bars for observed dissolution rates fall inside the symbols.

Figure 9 Cartoon showing the sequence of steps occurring during the APR16-D1Ab experiment, that from the dissolution lead to the formation of the new cpx. Insights show group 2-new cpx at t_1 and t_3 with the Fe-Mg partition coefficient between core, mantle and rim and the coexisting melt.

Figure 10 Selected zoned cpx crystals from Agnano Monte Spina eruption (Campi Flegrei; 4100 BP; de Vita et al. 1999); dark gray areas (Mg# 80-89), indicated with a yellow line, correspond to the portion of grain whose shape is attributable to crystal-resorption event.

Table captions

Table 1 Composition (wt.%) of APR16 rock sample, APR16GL starting material and cpx Ves

Table 2 Experimental run conditions, phase assemblages and cpx Ves features

Table 3 Clinopyroxene dissolution rates

Table 4 Experimental conditions and dissolution-crystallization of steps of the APR16-D1Ab experiment

Online Resource 1 contains the supplementary figures

Online Resource 2 contains the supplementary Movie 1

Movie 1 shows, in real time, the dissolution of the cpx Ves in the APR16GL melt at 2 GPa and ~1570 °C over a time duration of ~4 s. Details on the acquisition technique are reported in §*2.3 Ultrafast X-ray imaging with the Paris Edinburgh press*. Brightness and contrast were increased to make the cpx Ves more visible, given the low density contrast between the cpx Ves and the APR16GL melt. Noteworthy, during the Movie 1 it is possible to observe a variation in the cpx

Ves-melt contrast. In particular, during the first seconds of the Movie the dissolution process seems to occur at temperature above the liquidus of the APR16GL (T_L ~1460 °C at 2 GPa; Table 2) and below the liquidus of the cpx Ves (i.e., $T \leq 1597$ °C; Table 2) while after ~3 s the dissolution occurred at temperature near/above the cpx Ves liquidus temperature (i.e., $T \geq 1597$ °C). Considering the increase of T of 100 °C/s and the heat conduction in the experimental run probably in the first second of the Movie the T was < 1460 °C and it reaches $T \geq 1570$ °C at around 3 s. Furthermore, the temperature uncertainty is ~60 °C (Kono et al., 2014b), so it is very likely that the nominal temperature is higher ($\geq T$ liquidus of cpx Ves) in accordance with the complete disappearance of the cpx crystal observed in the Movie.

Online Resource 3 contains the supplementary tables

Online Resource 4 contains the Electronic Appendix

Figure 1

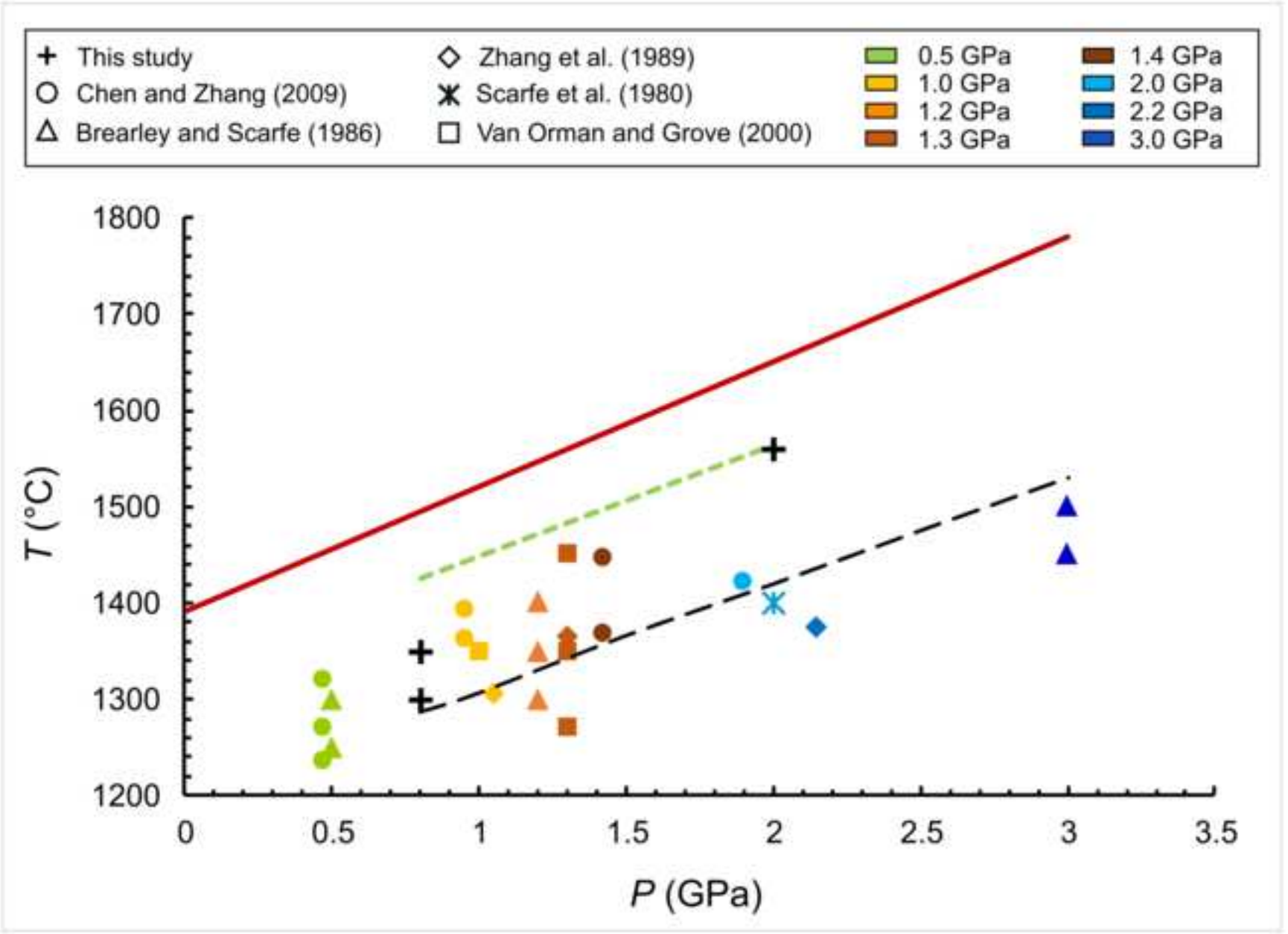

Figure 2

Click here to access/download;Figure;Figure 2.png

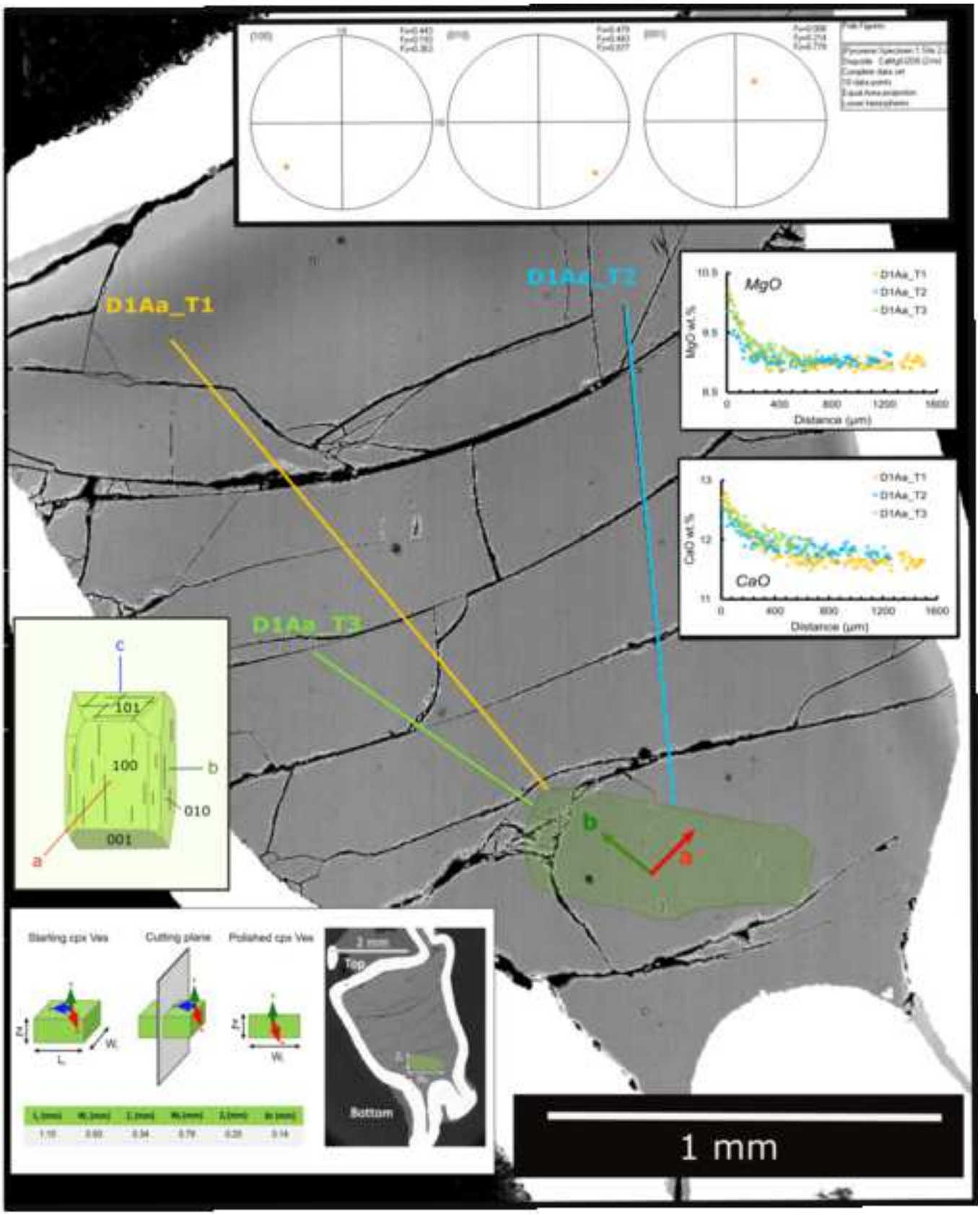

Figure 3

Click here to access/download;Figure;Figure 3.png

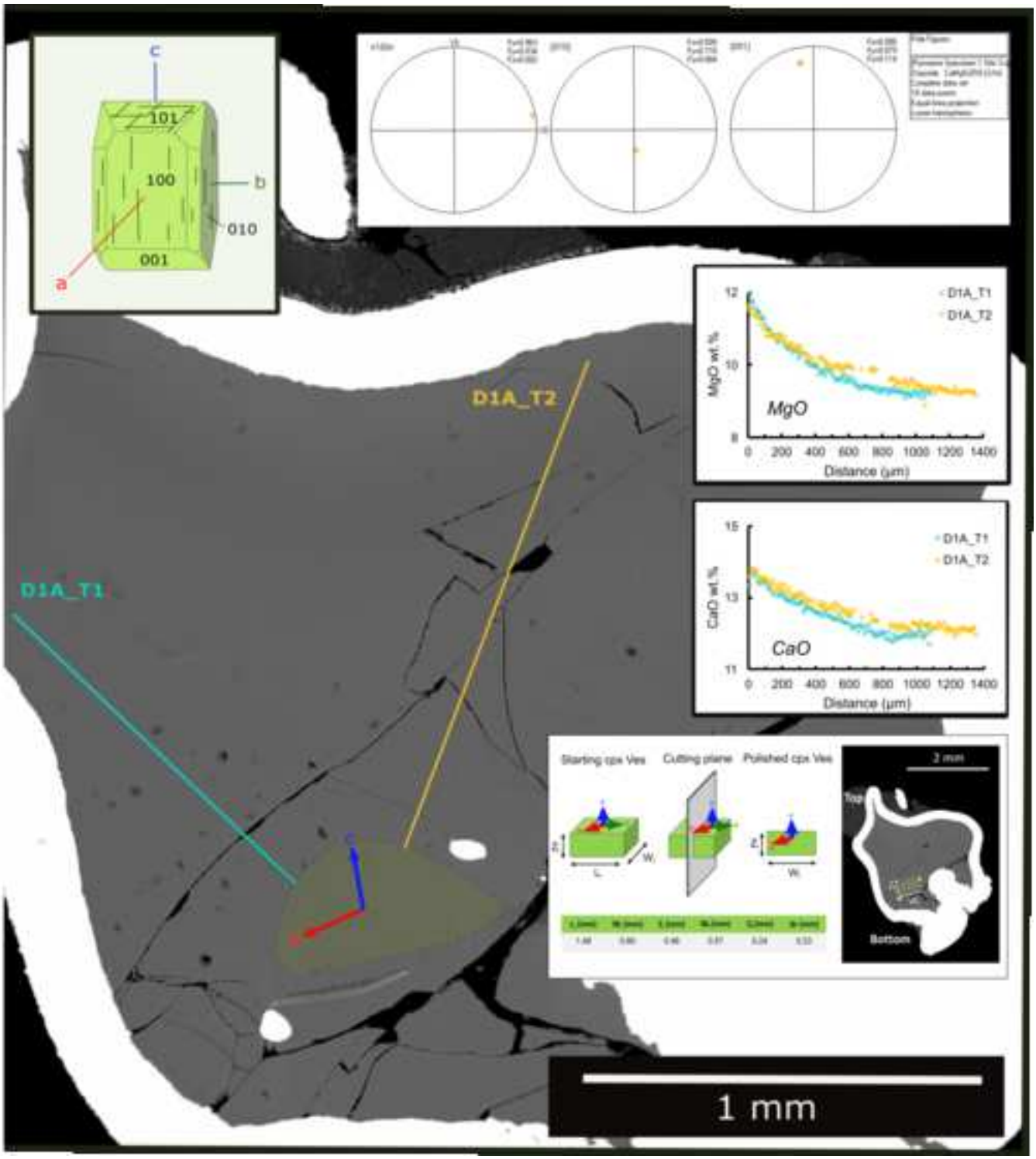

Figure 4

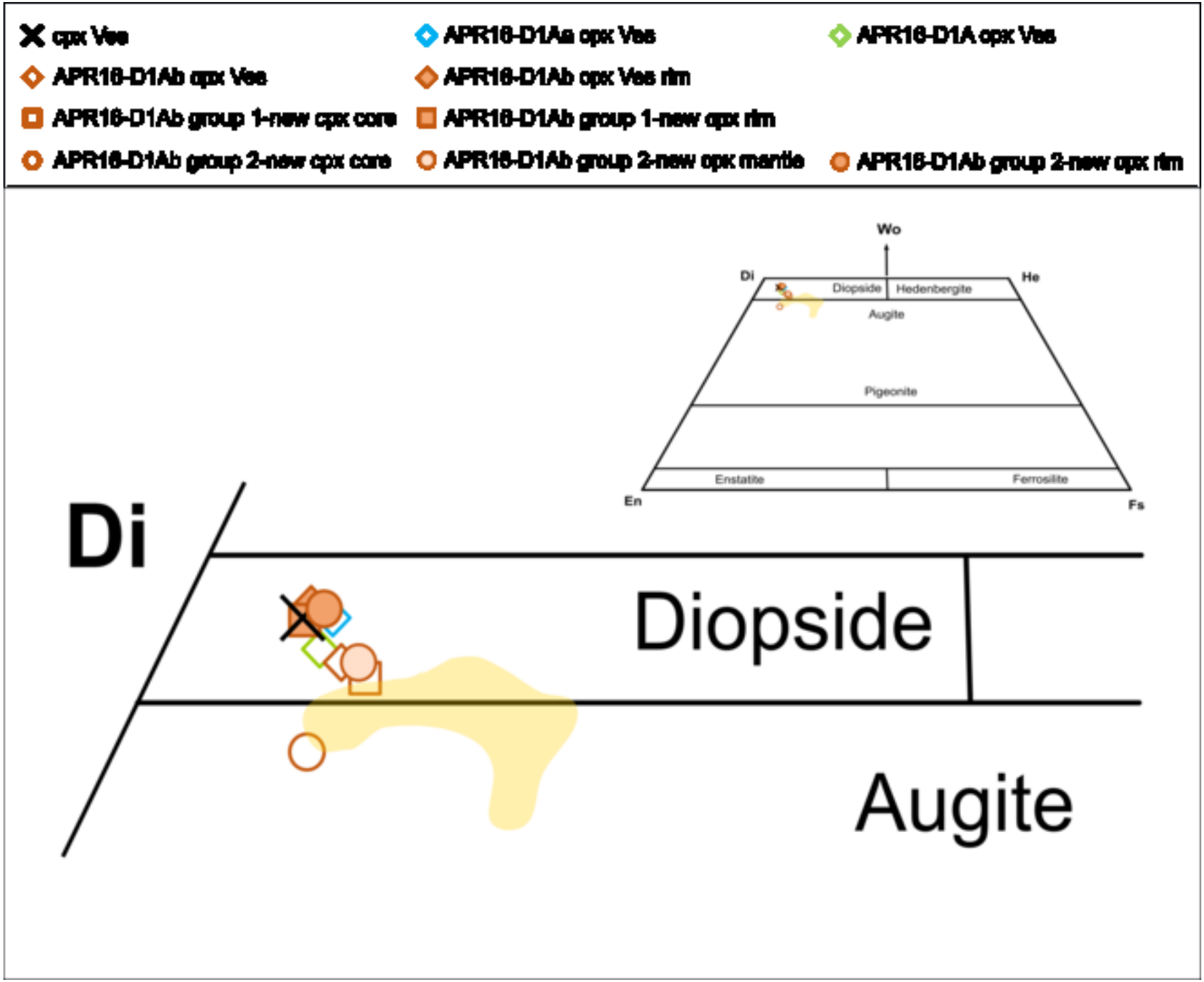

Figure 5

Click here to access/download;Figure;Figure 5.png

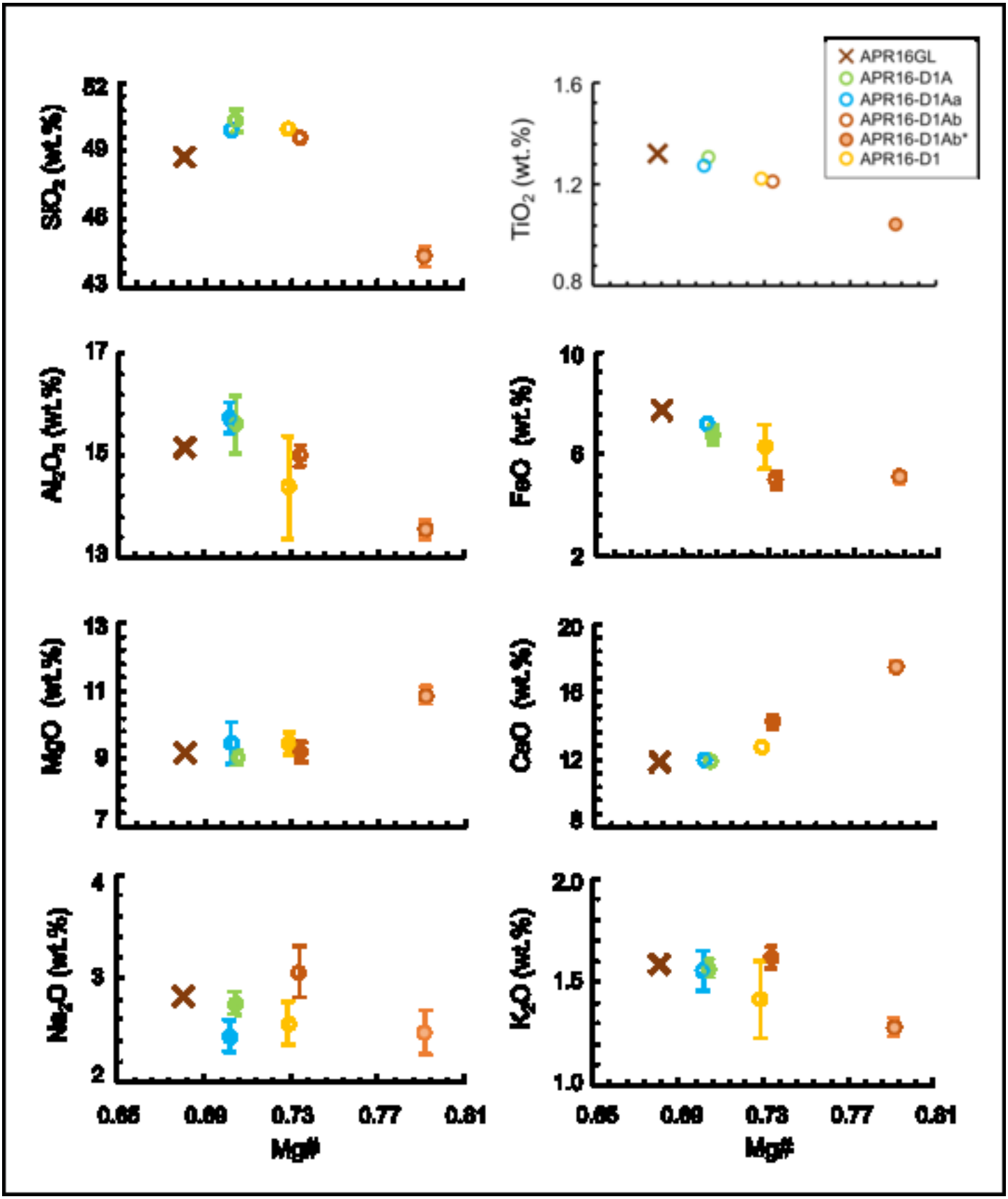

Figure 6

Click here to access/download;Figure;Figure 6.png

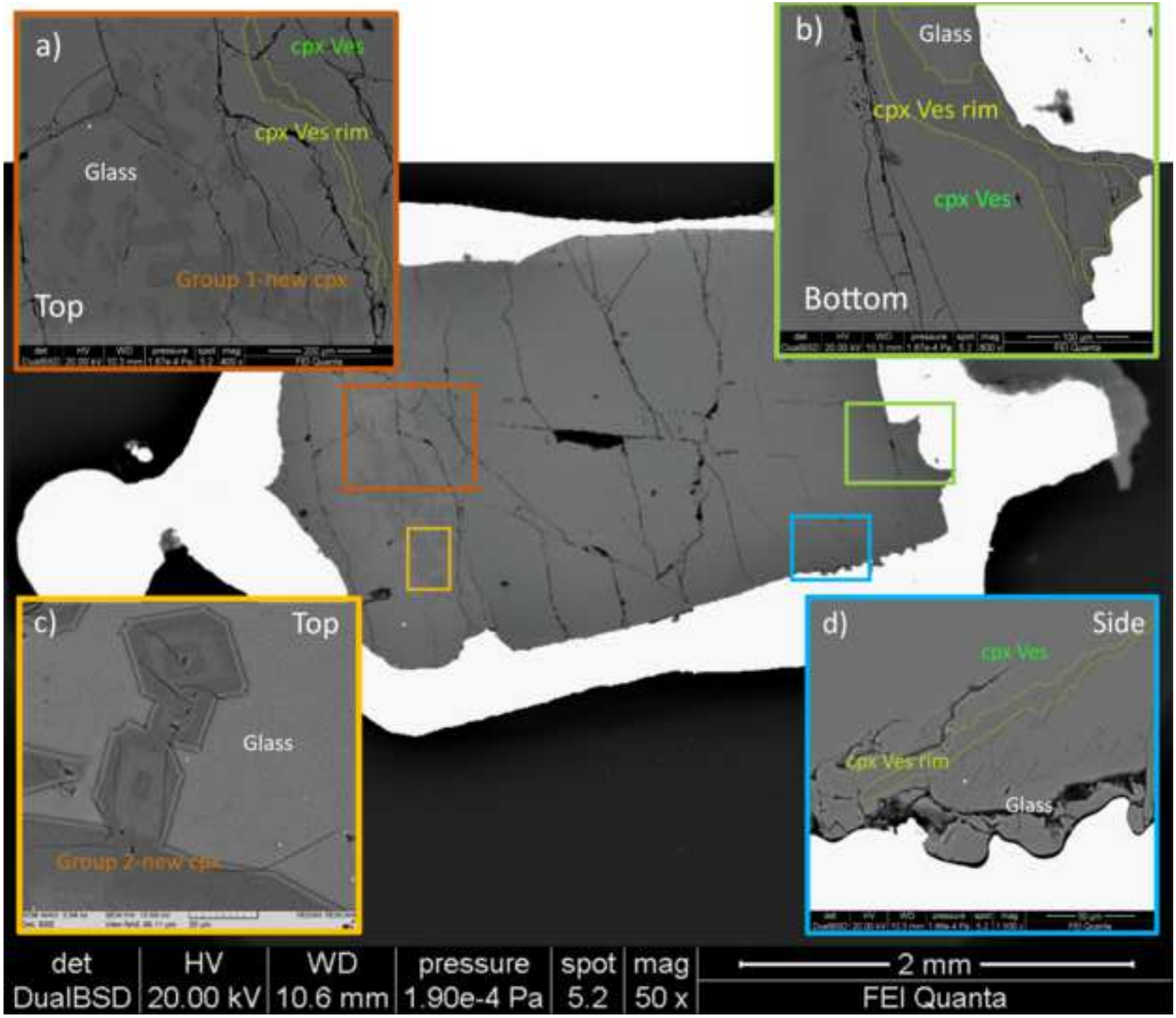

Figure 7

Click here to access/download;Figure;Figure 7.png

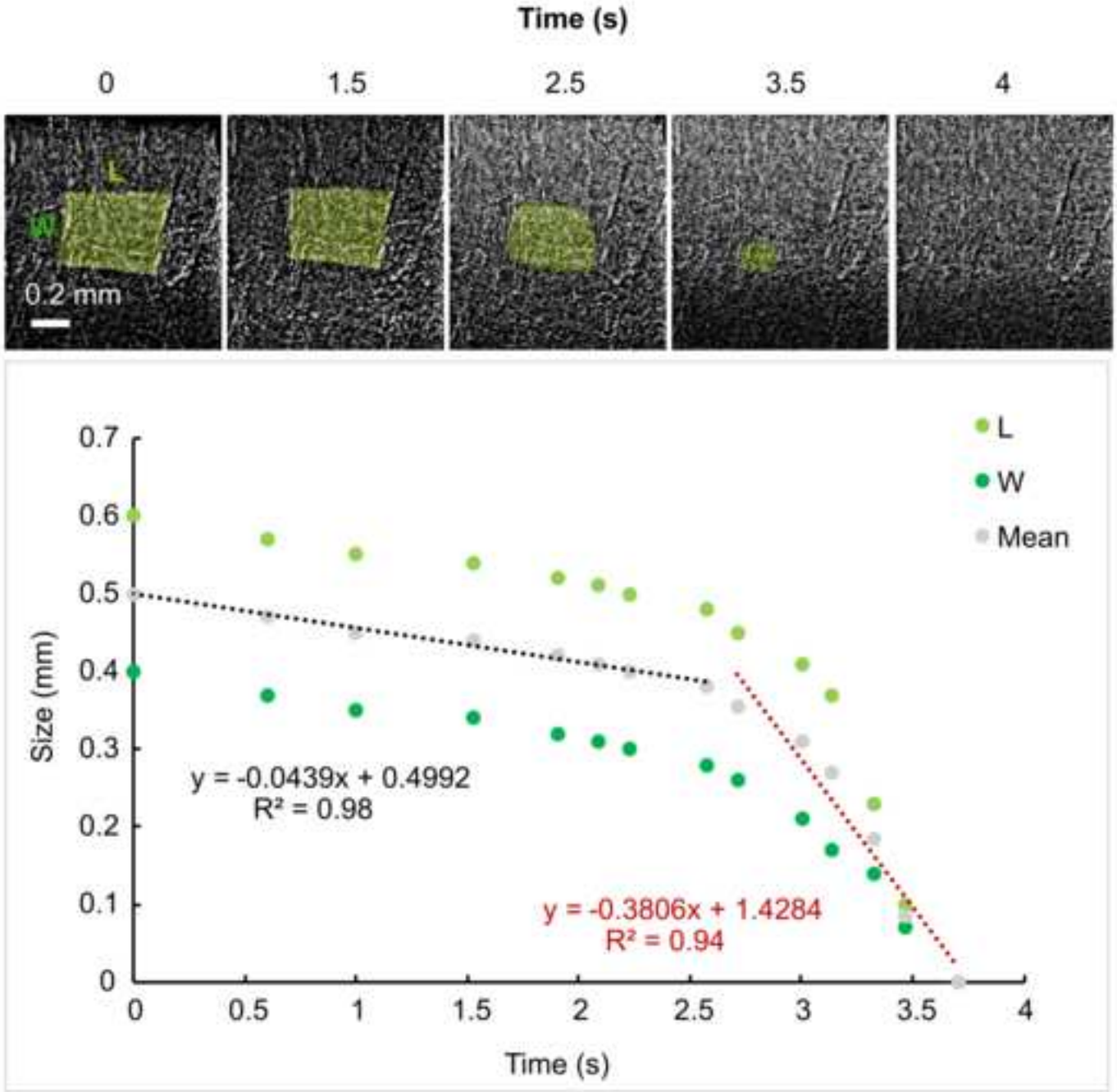

Figure 8

Click here to access/download;Figure;Figure 8_R2.png

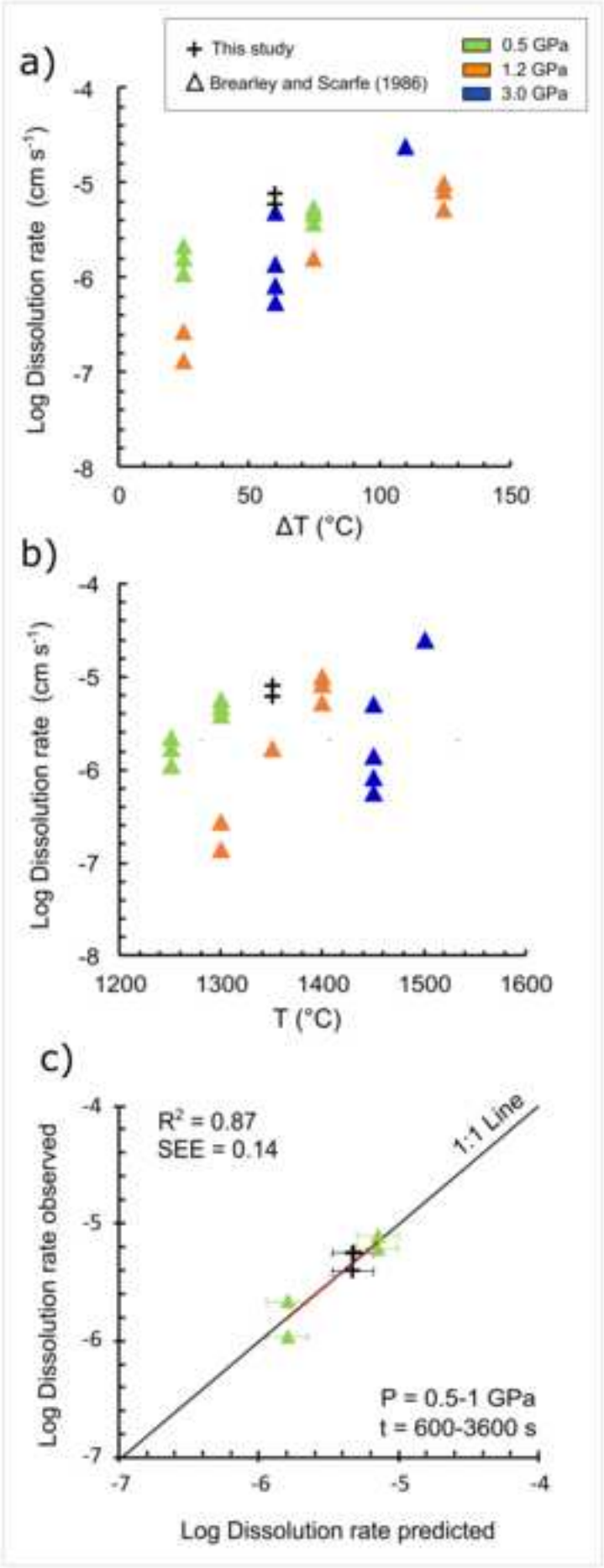

Figure 9

Click here to access/download;Figure;Figure 9.png

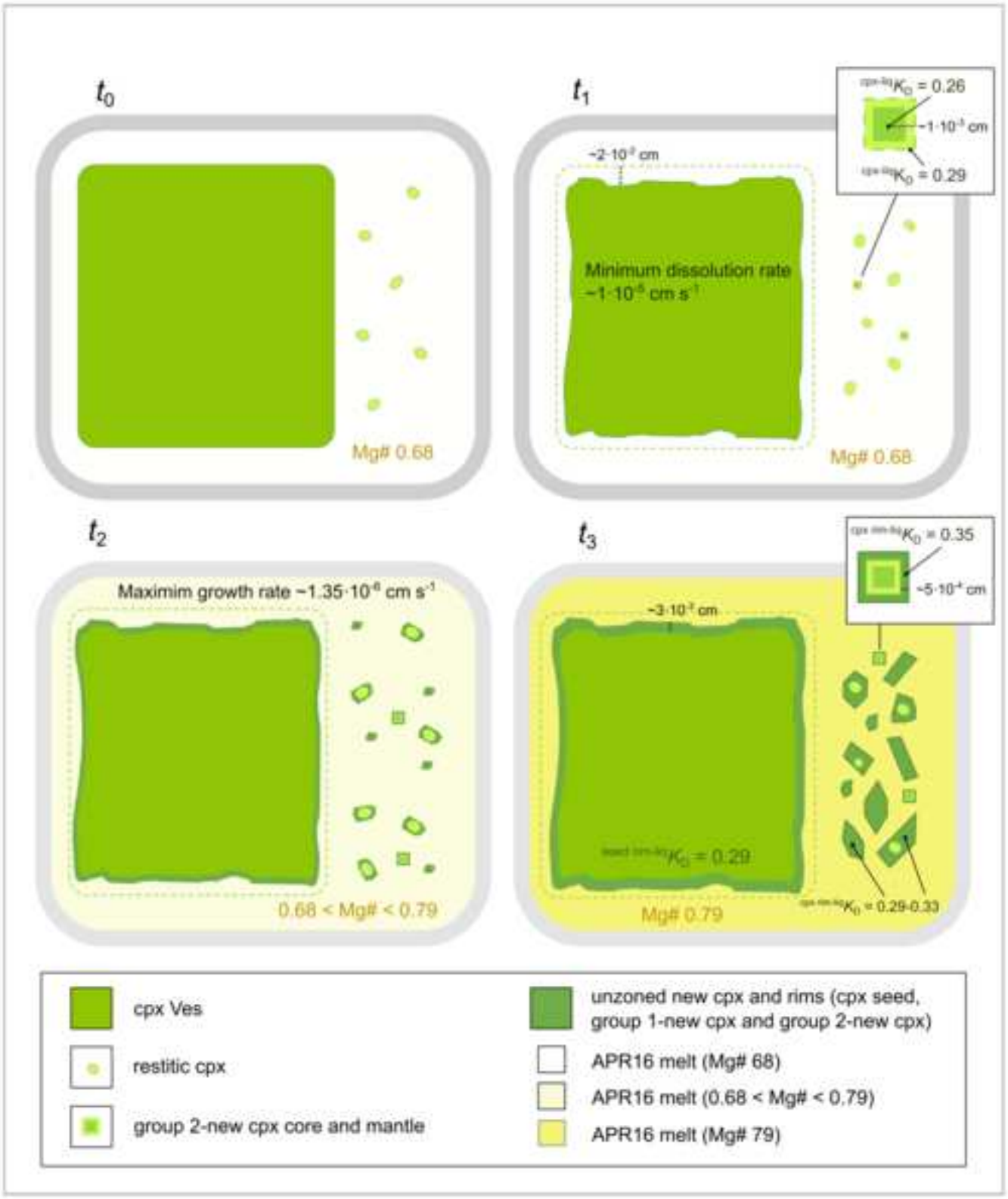

Figure 10

Click here to access/download;Figure;Figure 10.png

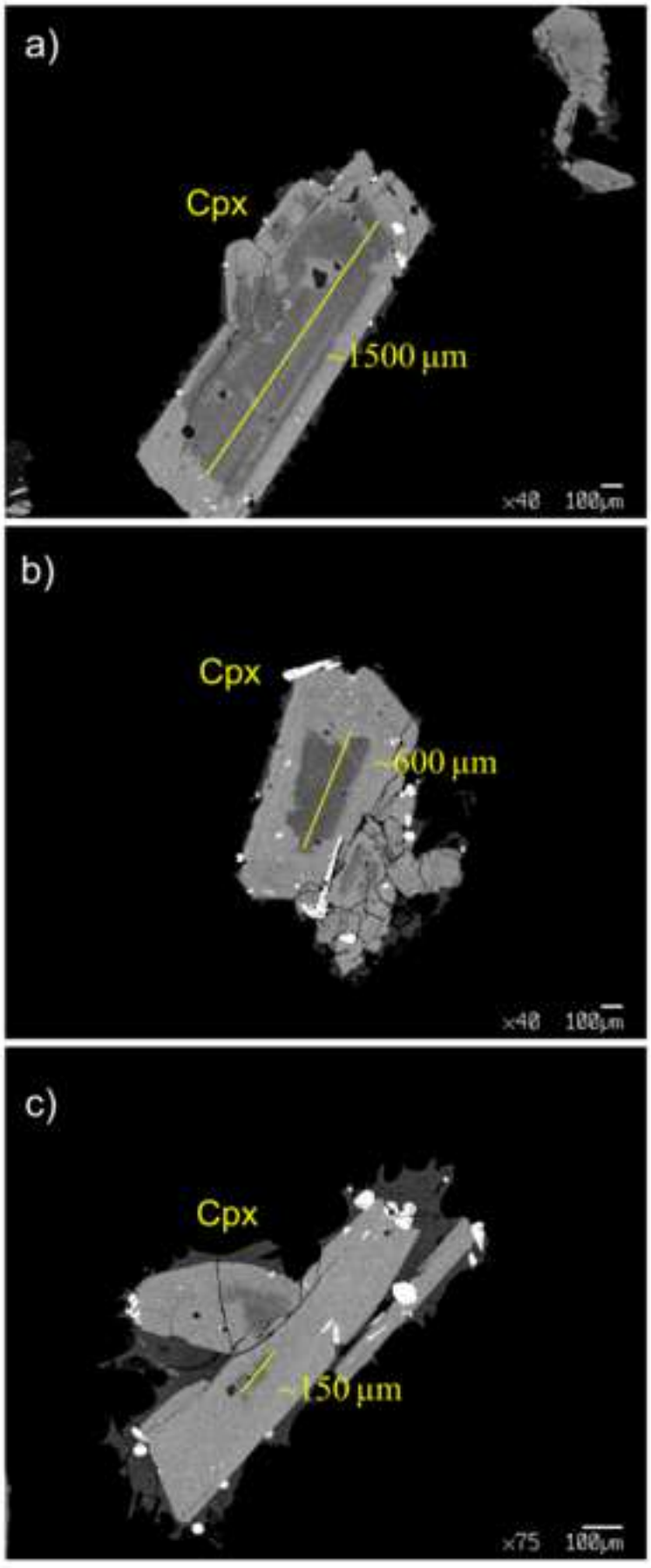

Table 1 Composition (wt.%) of APR16 rock sample, APR16GL starting material and cpx Ves

Sample	APR16	APR16GL	Cpx Ves*
SiO_2	48.89	49.30 (0.46)	53.27 (0.33)
TiO_2	1.23	1.33 (0.03)	0.40 (0.03)
Al_2O_3	15.65	15.31 (0.14)	2.19 (0.15)
FeO_{tot}	8.08	7.79 (0.13)	3.56 (0.22)
MnO	0.14	0.14 (0.05)	0.08 (0.04)
MgO	8.89	9.31 (0.07)	16.79 (0.17)
CaO	11.64	12.02 (0.09)	24.63 (0.18)
Na_2O	2.88	2.86 (0.05)	0.14 (0.01)
K_2O	1.52	1.60 (0.02)	-
P_2O_5	0.31	0.55 (0.02)	-
Cr_2O_3	-	-	0.27 (0.14)
L.O.I.	0.61	-	
Total	99.23	99.31 (0.29)[y]	101.39
Mg#[1]	0.66	0.68	0.89
T_L (°C)	1280	1290	
Wo			48
En			46
Fs			6

[1][MgO/(MgO+FeO_{tot})] molar, assuming all iron as FeO. APR16 composition from D'Antonio et al. (1999); APR16GL composition from Perinelli et al. (2019). Compositions are normalized to 100. Standard deviation is reported in parenthesis.
*Representative analysis of cpx from this study. Abbreviation: Cpx clinopyroxene; Wo wollastonite; En enstatite; Fs ferrosilite. T_L liquidus temperature (Perinelli et al., 2019).

Table 2 Experimental run conditions, phase assemblages and cpx Ves features

Run#	Experimental device	Starting material	P (GPa)	T (°C)	T_L (°C)	ΔT (°C)	Time (s)	Phases	$T_{cpx\ liquidus}$ (°C)	Cpx Ves size (L x W x Z; mm)	Cpx Ves weight (g)	Powder/cpx Ves ratio
APR16-D1	PE	APR16GL	2	1570	1460	110	4	Gl	1597	0.60 x 0.40 x 0.31	0.0004	n.d.
APR16-D1A	PC	APR16GL	0.8	1350	1290	60	3600	Gl + cpx* + ol + ox	1425	1.48 x 0.80 x 0.46	0.0008	0.95
APR16-D1Aa	PC	APR16GL	0.8	1350	1290	60	1800	Gl + cpx*	1425	1.10 x 0.93 x 0.34	0.0009	0.96
APR16-D1Ab	PC	APR16	0.8	1300	1280	20	7200	Gl + cpx* + cpx	1425	2.32 x 2.19 x 1.43	0.0238	0.59

PE = Paris-Edinburgh press; PC = piston cylinder apparatus; ΔT is difference between the nominal temperature of the runs and the APR16/APR16GL liquidus temperature (T_L; Table 1); $T_{cpx\ liquidus}$ is the liquidus temperature of the cpx Ves. Liquidus temperatures for both glass and cpx were calculated using the software MELTS (Asimow and Ghiorso, 1998; Gualda et al., 2012); *cpx Ves used for the experiments. Ol and Ox crystallized in APR16-D1A run occur in a small reservoir present in one side of the capsule.

Table 4 Experimental conditions and dissolution-crystallization of steps of the APR16-D1Ab experiment

<table>
<tr><th colspan="5">Experimental conditions</th></tr>
<tr><td colspan="2">Starting material</td><td colspan="3">Cpx Ves (a low pressure cpx from 1944 Vesuvius eruption) + APR16 (powdered natural rock with restitic cpx+ol)</td></tr>
<tr><td colspan="2">Pressure</td><td colspan="3">0.8 GPa</td></tr>
<tr><td colspan="2">Temperature</td><td colspan="3">1300 °C</td></tr>
<tr><td colspan="2">Powder/cpx Ves weight ratio</td><td colspan="3">0.59</td></tr>
<tr><td colspan="2">Estimated liquidus temperature of APR16+cpx Ves bulk composition (Mg# = 0.83)*</td><td colspan="3">1384 °C</td></tr>
<tr><td colspan="2">Total duration</td><td colspan="3">2 h</td></tr>
<tr><th colspan="5">Timing of experimental processes</th></tr>
<tr><td colspan="2">Time</td><td colspan="2">cpx Ves</td><td>APR16 powdered rock</td></tr>
<tr><td colspan="2">t_0</td><td colspan="2">Instability of the cpx Ves</td><td>Dissolution + restitic cpx crystals</td></tr>
<tr><td>t_1</td><td>~0.5 h</td><td>Dissolution of ~0.02 cm</td><td>Cation diffusion in the melt is limited and does not change the APR16 composition</td><td>Crystallization of the core + mantle of group 2-new cpx (~10 µm) in local equilibrium with the APR16 composition (Mg# ~0.68)</td></tr>
<tr><td rowspan="2">t_2</td><td rowspan="2">→1.5 h</td><td colspan="3">Cation diffusion produces progressive change of APR16 composition (Mg# changes from ~0.68 to ~0.80)</td></tr>
<tr><td colspan="2">End of cpx Ves dissolution and formation of the overgrowth rim</td><td>Overgrowth rims develop on 1) group 2-new cpx cores and on 2) restitic APR16-cpx.
Formation of new unzoned cpx</td></tr>
<tr><td>t_3</td><td>quench</td><td colspan="2">~30-µm-thick cpx Ves rim developed</td><td>1) ~70 µm-thick of rims developed on both type of zoned new cpx;
2) unzoned new cpx have reached a maximum size of ~200 µm</td></tr>
</table>

Notes: * the APR16+cpx Ves bulk composition has been calculated on the basis of the powder/cpx Ves ratio. Liquidus temperatures are determined by the MELTS code (Ghiorso and Sack, 1995; Asimow and Ghiorso, 1998).